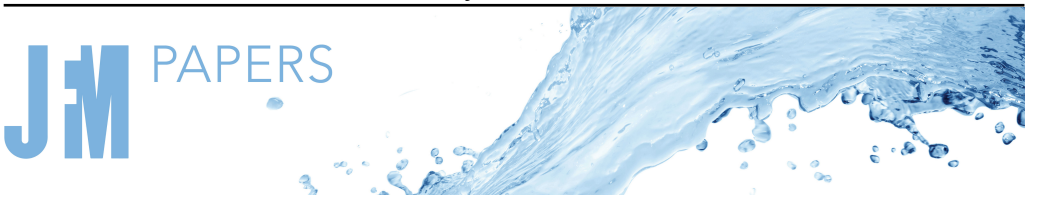
J. Fluid Mech. (2025), *vol.* 1021, A50, doi:10.1017/jfm.2025.10754



Dynamics of an internally actuated weakly elastic sphere translating parallel to a rigid wall

Shashikant Verma[1], **Bhagavatula Dinesh**[2] and **Navaneeth Kizhakke Marath**[1,3]

[1]Department of Mechanical Engineering, Indian Institute of Technology Ropar, 140001, India

[2]Department of Chemical Engineering and Technology, Indian Institute of Technology (BHU), Varanasi, 221005, India

[3]Centre of Research for Energy Efficiency and Decarbonization (CREED), Indian Institute of Technology Ropar, 140001, India

Corresponding author: Navaneeth Kizhakke Marath, navaneeth@iitrpr.ac.in

(Received 26 April 2025; revised 22 September 2025; accepted 22 September 2025)

We analyse the dynamics of a weakly elastic spherical particle translating parallel to a rigid wall in a quiescent Newtonian fluid in the Stokes limit. The particle motion is constrained parallel to the wall by applying a point force and a point torque at the centre of its undeformed shape. The particle is modelled using the Navier elasticity equations. The series solutions to the Navier and the Stokes equations are used to obtain the displacement and velocity fields in the solid and fluid, respectively. The point force and the point torque are calculated as series in small parameters α and $1/H$, using the domain perturbation method and the method of reflections. Here, α is the measure of elastic strain induced in the particle resulting from the fluid's viscous stress and H is the non-dimensional gap width, defined as the ratio of the distance of the particle centre from the wall to its radius. The results are presented up to $O(1/H^3)$ and $O(1/H^2)$, assuming $\alpha \sim 1/H$, for cases where gravity is aligned and non-aligned with the particle velocity, respectively. The deformed shape of the particle is determined by the force distribution acting on it. The hydrodynamic lift due to elastic effects (acting away from the wall) appears at $O(\alpha/H^2)$ in the former case. In an unbounded domain, the elastic effects in the latter case generate a hydrodynamic torque at $O(\alpha)$ and a drag at $O(\alpha^2)$. Conversely, in the former case, the torque is zero, while the drag still appears at $O(\alpha^2)$.

Key words: low-Reynolds-number flows, suspensions

© The Author(s), 2025. Published by Cambridge University Press.

https://doi.org/10.1017/jfm.2025.10754 Published online by Cambridge University Press

1. Introduction

Quantifying the hydrodynamic force and torque acting on a particle moving in confined flows is crucial for various industrial and biological applications such as the separation of cells in microfluidic devices (Secomb *et al.* 1986; Wu *et al.* 2021; Song, Li & Xuan 2023). In many of these applications, the ambient flow is predominantly unidirectional. In such flows, it is well known that a rigid spherical particle does not experience lateral movement in the Stokes limit due to the Stokes reversibility (Guazzelli & Morris 2011). Many analytical studies have examined the dynamics of the particle near a rigid wall and found no lateral movement in the Stokes regime (Dean & O'Neill 1963; O'Neill 1964; Goldman *et al.* 1967). However, the particle can move laterally due to nonlinear effects like inertia (finite Reynolds number flows) and fluid non-Newtonian properties (Matas, Morris & Guazzelli 2004). In shear flow, the inertial effects can induce lateral migration of the particle through three distinct contributions: (i) due to the slip velocity of the particle (Saffman 1965); (ii) due to the interactions with the wall; and (iii) due to the gradient in the ambient shear flow (Ho & Leal 1974; Vasseur & Cox 1976; Anand & Subramanian 2023). These contributions explain several experimental observations, including the Segre–Siberberg effect (Segre & Silberberg 1961; Matas *et al.* 2004; Nakayama *et al.* 2019). In contrast, a deformable particle, such as a spherical drop/bubble in wall-bounded flows, exhibits lateral migration even in the Stokes regime due to deformation-induced wall lift force (Leal 1980). In a single wall-bounded linear shear flow, a neutrally buoyant spherical drop exhibits migration away from the wall at a rate varying inversely to the square of the distance between the wall and the drop (Chaffey, Brenner & Mason 1965). In general, a drop of arbitrary density and viscosity experiences an inertial-induced and deformation-induced wall lift force while translating next to a rigid wall (Magnaudet, Takagi & Legendre 2003). The dynamics of a rigid particle moving next to a flexible surface has been analysed using analytical, numerical and experimental methods (Urzay *et al.* 2007; Saintyves *et al.* 2016; Rallabandi *et al.* 2018; Bertin *et al.* 2022; Rallabandi 2024). The lift force on a rigid cylinder and sphere moving near an elastic wall has been estimated in the Stokes limit (Rallabandi *et al.* 2017; Daddi-Moussa-Ider *et al.* 2018). Elastohydrodynamic interactions between soft material-coated interfaces have been studied within the lubrication approximation (Sekimoto & Leibler 1993; Skotheim & Mahadevan 2005). The lift force has been evaluated for various geometrical configurations, including: a rigid cylinder moving parallel to a soft-coated rigid substrate, a soft cylinder moving parallel to a rigid substrate, a cylindrical shell moving parallel to a rigid substrate and a cylindrical journal bearing coated with a soft layer (Skotheim & Mahadevan 2005). In all the configurations, the soft material has been modelled as a linear elastic, compressible solid governed by Navier elasticity equations. Further, the influence of substrate viscoelasticity on the lift force experienced by a rigid sphere translating parallel to a soft surface has been studied analytically in the lubrication limit (Kargar-Estahbanati & Rallabandi 2021).

In the Stokes limit, the lateral movement/lift force observed when either the wall or the particle is deformable arises due to a breakdown of the Stokes reversibility. The effects of particle deformability have been extensively studied through numerical simulations, particularly for vesicles, capsules and drops (Doddi & Bagchi 2009; Nix *et al.* 2014; Barthes-Biesel 2016; Bureau *et al.* 2023). However, modelling the particle as an elastic solid rather than a drop alters its dynamics due to differences in their constitutive equations. Recent experiments have demonstrated that wall effects suppress the terminal velocity of an elastic particle, whereas its deformability enhances it (Noichl & Schönecker 2022). To model elasticity, one can use Hooke's law for small deformations and the Neo-Hookean model (Li *et al.* 2020) for finite deformations. Theoretical studies have showed

https://doi.org/10.1017/jfm.2025.10754 Published online by Cambridge University Press

that the dynamic behaviour of the particle is sensitive to the chosen model; for instance, in an unbounded domain, a compressible Hookean sphere exhibits enhanced terminal velocity (Murata 1980), whereas an incompressible Neo-Hookean sphere experiences a reduction in terminal velocity compared with the corresponding Stokes velocity (Nasouri, Khot & Elfring 2017). The dynamics of rigid spheres, vesicles, capsules and drops near walls are well studied, but analytical investigations of wall effects on elastic solids remain limited. Most analytical studies have focused on elastic solids moving in an unbounded domain (Tam & Hyman 1973; Murata 1980), leaving a knowledge gap in wall interaction effects. For a rigid sphere moving near a rigid wall, analytical techniques using bispherical harmonics (O'Neill 1964), lubrication theory (Goldman *et al.* 1967) and the method of reflections (Kim & Karrila 2013) provide solutions in the Stokes limit. The results from the method of reflections for the sphere align well with experimental data for wall–particle gap widths greater than 1.5 (translation) and 1.3 (rotation) (Małysa & Van De Ven 1986). Further, it has been observed numerically that at low capillary number, defined as the ratio of viscous and elastic forces, the lift velocity of a capsule in a bounded simple shear flow is nearly equal to the analytical solution (based on far-field approximation) over a wide range of wall–particle gap widths (Nix *et al.* 2014). Therefore, we use the method of reflections in this work to analyse the wall effects on the dynamics of an elastic particle for two cases: first, when the gravity is aligned with particle velocity and second, when the gravity is in an arbitrary direction. The particle is considered as a weakly elastic sphere that translates parallel to a rigid wall. We model the particle using Navier elasticity equations and the fluid using Stokes equations. An external point force and a point torque are applied to constrain the motion of the particle parallel to the wall as shown in figure 1(*a*).

The concept of the point force applied at the centre of a particle is relevant to physical systems such as smart polymeric beads, particularly magnetoresponsive polymer beads (Philippova *et al.* 2011). These beads typically consist of a polymer matrix embedded with magnetic nano- or microparticles (MPs), where the polymer imparts structural stability and elasticity. Such systems are used in biomedical applications – for instance, in the *in vitro* magnetic separation of biological cells. Non-magnetic particles can be bound to magnetically responsive beads for manipulation via magnetic fields (Safarik, Safarikova & Forsythe 1995; Safarikova & Safarik 2001; Philippova *et al.* 2011). The magnetic particles may be distributed either uniformly or non-uniformly within the polymer matrix (Kim *et al.* 2005; Peng *et al.* 2008; Philippova *et al.* 2011). The schematic of encapsulated MPs inside the polymer bead is shown in figure 1(*b*). The average number of MPs per polymer bead can be tuned by adjusting the concentrations of the polymer and MPs (Kim *et al.* 2005). The response of each embedded magnetic particle inside a bead to the external magnetic field can be interpreted as a localised force. Although the magnetic field is distributed over the finite region occupied by the magnetic particle, its small size relative to the bead allows this force to be effectively approximated as a point force. Such a bead can also experience localised torque when exposed to a rotating magnetic field (Moerland, Van IJzendoorn & Prins 2019). In our analysis, we considered the simplest model for the bead in which a point force and a point torque are positioned at the centre of an elastic sphere.

The problem set-up in the present analysis corresponds to a resistance problem, in which the forces and the torques required to achieve a specified motion are determined. Murata solved the mobility problem for a weakly elastic sphere sedimenting under gravity in an unbounded domain (Murata 1980). In a mobility problem, the motion of the particle is determined for a given set of forces and torques (Kim & Karrila 2013). For a rigid particle, the results from the mobility problem can be used to derive those of the resistance problem. However, such a relationship need not hold for a deformable particle. For a deformable

https://doi.org/10.1017/jfm.2025.10754 Published online by Cambridge University Press

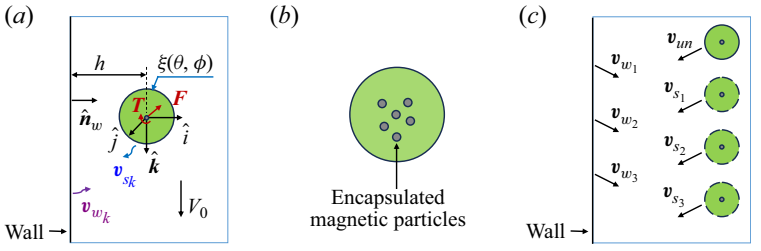


Figure 1. (*a*) Schematic of an elastic sphere translating parallel to a rigid wall at a specified velocity ($V_0\hat{\boldsymbol{k}}$), subjected to an external point force ($\boldsymbol{F}$) and a point torque ($\boldsymbol{T}$). (*b*) Schematic of the Fe_3O_4 nanoparticles encapsulated within the PDMS matrix (Peng *et al.* 2008). (*c*) Unbounded velocity field ($\boldsymbol{v}_{un}$) undergoing subsequent reflections from wall (w) and sphere (s).

particle, its shape depends on the force distribution acting on it, which can differ between the mobility and resistance problems. Murata's results are for a specific force distribution that arises from the balance of gravity and hydrodynamic forces. However, the force distribution in our case is different and, hence, we cannot use his results for our analysis in an unbounded domain. Therefore, we first analyse the motion of the particle in an unbounded domain as a resistance problem and subsequently account for the wall effects using the method of reflections. We use a theoretical approach similar to that used in Murata's work, employing domain perturbation and series solutions for the governing equations of both the particle and fluid. The deformed shape we obtain for the first case (gravity aligned with particle velocity) differs from that obtained in Murata's work, due to the difference in the force distribution in both problems. Our analysis of the unbounded problem in the second case (gravity is in an arbitrary direction) reveals that hydrodynamic forces acting along the translational direction are modified by body forces acting perpendicular to the motion. The wall effects on particle dynamics are analysed using the method of reflections. In the method, the disturbance velocity field generated by the particle's motion in an unbounded domain is iteratively reflected between the wall and particle surfaces to satisfy boundary conditions on both. Reflections are carried out to obtain results up to $O(1/H^3)$ and $O(1/H^2)$ for the first and the second cases, respectively, assuming α is of the order $1/H$. The importance of this assumption that simplifies the analysis is discussed in § 3.1. Hydrodynamic forces due to wall effects generate a lift force away from the wall. We find that the point force balancing the lift is non-zero in the first case and zero in the second. Further, we find that the point torque is zero in the first case but non-zero in the second.

The subsequent sections of this manuscript are organised as follows. Section 2 presents the mathematical formulation, the governing equations and the boundary conditions. The results are presented for the first and second case in § 3.1 and § 3.2, respectively. The results for a neutrally buoyant particle and for zero gravity are presented in § 3.1. We summarise our investigation in § 4.

2. Mathematical formulation

We consider a weakly elastic spherical particle of undeformed radius (R_0) moving in a quiescent Newtonian fluid. The particle is translating parallel to a rigid wall at a velocity ($V_0\hat{\boldsymbol{k}}$), as shown in figure 1(*a*). The sphere centre is at a distance h from the wall. An external point force ($\boldsymbol{F}$) and a point torque ($\boldsymbol{T}$) are applied at the centre to ensure that its motion is parallel to the wall. The unit vector normal to the wall ($\hat{\boldsymbol{n}}_w$) is aligned with the x-axis. We assume that the inertial effects in the flow are negligible compared with the

https://doi.org/10.1017/jfm.2025.10754 Published online by Cambridge University Press

viscous effects, i.e. the Reynolds number, defined as $Re = \rho_f V_0 R_0/\mu \ll 1$. Here, ρ_f and μ are the fluid density and viscosity, respectively. We assume that the fluid is incompressible and is governed by the Stokes equations given by

$$-\nabla p + \mu \nabla^2 \boldsymbol{v} + \rho_f \boldsymbol{g} = 0, \tag{2.1}$$

$$\nabla \cdot \boldsymbol{v} = 0. \tag{2.2}$$

In (2.1) and (2.2), $\boldsymbol{v}$ and p are the velocity and pressure fields in the fluid, respectively, and $\boldsymbol{g}$ is the acceleration due to gravity. The particle is modelled using the Navier elasticity equations given by

$$[\lambda + G]\nabla\,(\nabla \cdot \boldsymbol{u}) + G\nabla^2 \boldsymbol{u} + \rho_p \boldsymbol{g} + \boldsymbol{F}\delta(\boldsymbol{x}) + \frac{1}{2}\,[\nabla\delta(\boldsymbol{x}) \times \boldsymbol{T}] = 0. \tag{2.3}$$

Here, $\boldsymbol{u}$ is the displacement field in the sphere, λ and G are the Lamé's constants, and ρ_p is the particle density. The fluid stress ($\boldsymbol{\sigma}$) is given by

$$\boldsymbol{\sigma} = -p\boldsymbol{I} + \mu\big(\nabla \boldsymbol{v} + [\nabla \boldsymbol{v}]^T\big) \tag{2.4}$$

and the solid stress ($\boldsymbol{\tau}$) is given by

$$\boldsymbol{\tau} = \lambda\,(\nabla \cdot \boldsymbol{u})\,\boldsymbol{I} + G\big(\nabla \boldsymbol{u} + [\nabla \boldsymbol{u}]^T\big). \tag{2.5}$$

The variables in the problem are non-dimensionalised using the scalings given as

$$\boldsymbol{v}^* = \frac{\boldsymbol{v}}{V_0}; \quad p^* = \frac{pR_0}{\mu V_0}; \quad \boldsymbol{\sigma}^* = \frac{\boldsymbol{\sigma} R_0}{\mu V_0}; \quad \boldsymbol{u}^* = \frac{\boldsymbol{u}}{R_0}; \quad \boldsymbol{\tau}^* = \frac{\boldsymbol{\tau}}{G}; \quad H^* = \frac{h}{R_0}. \tag{2.6}$$

The deformability can be quantified as a measure of elastic strain when subjected to viscous stress, defined as $\alpha = \mu V_0/(GR_0)$ (Finney *et al.* 2024). The parameter α can also be interpreted as an elastic capillary number, representing the ratio of viscous to elastic stress (Villone & Maffettone 2019), or as the ratio of viscous to elastic forces (Murata 1980, 1981; Nasouri *et al.* 2017). The ratio of the bulk modulus (λ) to the shear modulus (G) of the particle is denoted by γ; $\gamma = \lambda/G$. Non-dimensional variables are indicated using the asterisk symbol in (2.6), which is omitted hereafter for brevity.

To analyse the dynamics of the particle, we express the solutions of (2.1) and (2.3) in a spherical coordinate system (r,θ,ϕ), whose origin coincides with the centre of the undeformed particle. The solutions are expressed in terms of ξ, θ and ϕ, where ξ is the non-dimensional radial coordinate defined by $\xi = r/R_0$, θ and ϕ are the polar and azimuthal angles, respectively. Since the wall–particle gap width is constant, the particle deforms and reaches a steady shape whose surface radius is defined by

$$\xi = 1 + f(\theta, \phi). \tag{2.7}$$

Here, f quantifies the surface deformation and is a function of the polar and azimuthal angles. Note that in an unbounded domain, if gravity is aligned with the particle velocity, f is axisymmetric about the translation axis (Murata 1980). The function f is related to the displacement field in the particle. The equation that relates the displacement of a material point on the deformed surface to its location on the undeformed surface is obtained in terms of f as

$$1 = \big[1 + f - u_r|_{\xi=1+f(\theta,\phi)}\big]^2 + \big[u_\theta|_{\xi=1+f(\theta,\phi)}\big]^2 + \big[u_\phi|_{\xi=1+f(\theta,\phi)}\big]^2. \tag{2.8}$$

Equation (2.8) states that, for any point on the deformed surface, the magnitude of the difference between its current position and the displacement it experienced is equal to one. Since the particle is weakly deformable ($\alpha \ll 1$), its shape deviates slightly from the spherical shape. Noting that α is small, we have expanded all the variables in the problem

https://doi.org/10.1017/jfm.2025.10754 Published online by Cambridge University Press

as series in α and used the domain perturbation method (Johns & Narayanan 2002; Leal 2007) to transfer the boundary conditions from the deformed to the undeformed surface of the particle. This generates the modified boundary conditions at the undeformed surface. The series solutions to the governing equations in (2.1)–(2.3) are used to find the fields that satisfy the modified boundary conditions. To include the effect of the wall, we have used the method of reflections (Kim & Karrila 2013) and the fields at each order in α are expanded as a series in $1/H$, the inverse of the non-dimensional wall–particle gap width. The external point force and the point torque are calculated based on the derived velocity and displacement fields at each order. We present the series solutions to the Stokes equations and the Navier elasticity equations in the above-mentioned spherical coordinate system in §§ 2.1 and 2.2. We explain the domain perturbation method for the case of the particle translating in an unbounded domain in § 2.3. The case of the particle translating parallel to a wall is discussed in § 2.4. We summarise the steps to estimate the point force and the point torque in § 2.5. The results are presented in § 3.

2.1. *Series solution to Stokes equations*

The solutions to (2.1) and (2.2) are written in a general form as follows (Kim & Karrila 2013). The radial (v_r), tangential (v_θ) and azimuthal (v_ϕ) velocity components are given by

$$v_r = \sum_{n=1}^{\infty}\sum_{m=0}^{n}\left[\left(\frac{\xi^{-n}(n+1)}{2(2n-1)}P_n^m[A_{mn}\cos m\phi + \tilde{A}_{mn}\sin m\phi]\right)\right.$$
$$\left. -\left(\xi^{-n-2}(n+1)P_n^m\left[B_{mn}\cos m\phi + \tilde{B}_{mn}\sin m\phi\right]\right)\right], \tag{2.9}$$

$$v_\theta = \sum_{n=1}^{\infty}\sum_{m=0}^{n}\left[\left(\frac{\xi^{-n}(n-2)}{2n(2n-1)(2n+1)\sin\theta}\left[(n+1)(n+m)P_{n-1}^m - n(n-m+1)P_{n+1}^m\right]\right)\right.$$
$$\times\left[A_{mn}\cos m\phi + \tilde{A}_{mn}\sin m\phi\right]$$
$$-\left(\frac{\xi^{-n-2}}{(2n+1)\sin\theta}\left[(n+1)(n+m)P_{n-1}^m - n(n-m+1)P_{n+1}^m\right]\right)$$
$$\times\left[B_{mn}\cos m\phi + \tilde{B}_{mn}\sin m\phi\right]$$
$$\left.+\left(\frac{\xi^{-n-1}m}{\sin\theta}P_n^m\left[-V_{mn}\sin m\phi + \tilde{V}_{mn}\cos m\phi\right]\right)\right], \tag{2.10}$$

$$v_\phi = \sum_{n=1}^{\infty}\sum_{m=0}^{n}\left[\left(-\frac{\xi^{-n}(n-2)m}{2n(2n-1)\sin\theta}P_n^m\left[-A_{mn}\sin m\phi + \tilde{A}_{mn}\cos m\phi\right]\right)\right.$$
$$+\left(\frac{\xi^{-n-2}m}{\sin\theta}P_n^m\left[-B_{mn}\sin m\phi + \tilde{B}_{mn}\cos m\phi\right]\right)$$
$$+\left(\frac{\xi^{-n-1}}{(2n+1)\sin\theta}\left[(n+1)(n+m)P_{n-1}^m - n(n-m+1)P_{n+1}^m\right]\right)$$
$$\left.\times\left(V_{mn}\cos m\phi + \tilde{V}_{mn}\sin m\phi\right)\right], \tag{2.11}$$

respectively, and the pressure is given by

$$p = \xi\left[K_{fz}\cos\theta + K_{fx}\cos\phi\sin\theta + K_{fy}\sin\theta\sin\phi\right]$$
$$+\sum_{n=1}^{\infty}\sum_{m=0}^{n}\left[\xi^{-n-1}P_n^m\left(A_{mn}\cos m\phi + \tilde{A}_{mn}\sin m\phi\right)\right]. \tag{2.12}$$

https://doi.org/10.1017/jfm.2025.10754 Published online by Cambridge University Press

Here, $K_{fx} = \rho_f R_0^2 g_x/(\mu V_0)$, $K_{fy} = \rho_f R_0^2 g_y/(\mu V_0)$, $K_{fz} = \rho_f R_0^2 g_z/(\mu V_0)$ and $\boldsymbol{g} = g_x\hat{\boldsymbol{i}} + g_y\hat{\boldsymbol{j}} + g_z\hat{\boldsymbol{k}}$ in the Cartesian cordinate system. Additionally, P_n^m denotes $P_n^m(\cos\theta)$, the associated Legendre polynomial of order m and degree n. The constants, A_{mn}, $\tilde{A}_{mn}$, B_{mn}, $\tilde{B}_{mn}$, V_{mn} and $\tilde{V}_{mn}$, are determined from the no-slip boundary conditions at the surface of the particle.

2.2. *Series solution to Navier elasticity equations*

The solution to (2.3) is expressed in a general form as follows (Kushch 2013). The radial (u_r), tangential (u_θ) and azimuthal (u_ϕ) displacement components are given by

$$\begin{aligned}
u_r = {} & \frac{1}{4\pi\xi}\left[F_z\cos\theta + F_x\cos\phi\sin\theta + F_y\sin\theta\sin\phi\right] \\
& - \frac{2\gamma+7}{30(\gamma+2)}\xi^2\left[K_{pz}\cos\theta + K_{px}\cos\phi\sin\theta + K_{py}\sin\theta\sin\phi\right] \\
& + \sum_{n=0}^{\infty}\sum_{m=0}^{n}\left[\xi^{n+1}P_n^m\left(B_{mn}^1\cos m\phi + B_{mn}^0\sin m\phi\right)\right] \\
& + \sum_{n=1}^{\infty}\sum_{m=0}^{n}\left[\xi^{n-1}P_n^m\left(C_{mn}^1\cos m\phi + C_{mn}^0\sin m\phi\right)\right], \qquad (2.13) \\
u_\theta = {} & \frac{(3+\gamma)}{8\pi(2+\gamma)\xi}\left(-F_z\sin\theta + \cos\theta\left[F_x\cos\phi + F_y\sin\phi\right]\right) \\
& + \frac{1}{8\pi\xi^2}\left(T_y\cos\phi - T_x\sin\phi\right) + \frac{4\gamma+9}{30(\gamma+2)}\xi^2 \\
& \times\left[K_{pz}\sin\theta - \cos\theta\left(K_{px}\cos\phi + K_{py}\sin\phi\right)\right] \\
& + \frac{1}{\sin\theta}\left[\sum_{n=1}^{\infty}\sum_{m=0}^{n}\left(\frac{\xi^n m(2n+1)}{n(n+1)}P_n^m\left[-A_{mn}^1\sin m\phi + A_{mn}^0\cos m\phi\right]\right)\right] \\
& + \frac{1}{\sin\theta}\left[\sum_{n=1}^{\infty}\sum_{m=0}^{n}\left(\frac{\xi^{n+1}[\gamma(n+3)+(n+5)]}{(2n+1)(n+1)[\gamma n+(n-2)]}\left[n(n-m+1)P_{n+1}^m\right.\right.\right. \\
& \left.\left.\left. - (n+1)(n+m)P_{n-1}^m\right]\right)\left(B_{mn}^1\cos m\phi + B_{mn}^0\sin m\phi\right)\right] \\
& + \frac{1}{\sin\theta}\left[\sum_{n=1}^{\infty}\sum_{m=0}^{n}\left(\frac{\xi^{n-1}}{(2n+1)n}\left[n(n-m+1)P_{n+1}^m - (n+1)(n+m)P_{n-1}^m\right]\right)\right. \\
& \left.\times\left(C_{mn}^1\cos m\phi + C_{mn}^0\sin m\phi\right)\right] \text{ and} \qquad (2.14) \\
u_\phi = {} & \frac{(3+\gamma)}{8\pi(2+\gamma)\xi}\left(F_y\cos\phi - F_x\sin\phi\right) - \frac{4\gamma+9}{30(\gamma+2)}\xi^2\left[K_{py}\cos\phi - K_{px}\sin\phi\right] \\
& + \frac{1}{8\pi\xi^2}\left(T_z\sin\theta - \cos\theta\left[T_x\cos\phi + T_y\sin\phi\right]\right) \\
& + \frac{1}{\sin\theta}\left[\sum_{n=0}^{\infty}\sum_{m=0}^{n}\left(\frac{-\xi^n}{(n+1)}\left[(n-m+1)P_{n+1}^m(A_{mn}^1\cos m\phi + A_{mn}^0\sin m\phi)\right]\right)\right.
\end{aligned}$$

https://doi.org/10.1017/jfm.2025.10754 Published online by Cambridge University Press

$$+\sum_{n=1}^{\infty}\sum_{m=0}^{n}\left(\frac{\xi^n}{n}\left[(n+m)P_{n-1}^m(A_{mn}^1\cos m\phi+A_{mn}^0\sin m\phi)\right]\right)\Bigg]$$
$$+\frac{1}{\sin\theta}\left[\sum_{n=0}^{\infty}\sum_{m=0}^{n}\left(\frac{\xi^{n+1}m[\gamma(n+3)+(n+5)]}{(n+1)[\gamma\, n+(n-2)]}P_n^m\left[-B_{mn}^1\sin m\phi+B_{mn}^0\cos m\phi\right]\right)\right]$$
$$+\frac{1}{\sin\theta}\left[\sum_{n=1}^{\infty}\sum_{m=0}^{n}\left(\frac{\xi^{n-1}m}{n}P_n^m\left[-C_{mn}^1\sin m\phi+C_{mn}^0\cos m\phi\right]\right)\right], \tag{2.15}$$

respectively. Here, $K_{px}=\rho_p g_x R_0/G$, $K_{py}=\rho_p g_y R_0/G$ and $K_{pz}=\rho_p g_z R_0/G$. The constants, A_{mn}^1, A_{mn}^0, B_{mn}^1, B_{mn}^0, C_{mn}^1 and C_{mn}^0, are determined from the stress continuity at the particle surface. The displacement field for the point force and the point torque decays as $1/\xi$ and $1/\xi^2$, respectively, as discussed in Appendix A. The Cartesian components of the force and torque are denoted by F_i and T_i $(i=x,\,y,\,z)$, respectively. We have done the analysis in a particle-fixed coordinate system and the point torque arrests the rotation of the particle. The constants that correspond to translation (C_{01}^1, C_{11}^1 and C_{11}^0) and rotation (A_{01}^1, A_{11}^1, and A_{11}^0) in the above-mentioned series are, therefore, set to zero.

2.3. *Domain pertubation method*

In this section, we describe the domain perturbation method that is used to transfer the boundary conditions from the deformed surface of the particle to the undeformed surface as it translates in an unbounded domain. The particle deforms as it translates in the quiescent fluid. Since the particle is weakly deformable, its shape deviates slightly from the spherical shape. The deformation f given in (2.7) has to be determined, as a part of the solution. The velocity boundary condition (no-slip) and the stress continuity on the deformed surface are given by

$$\boldsymbol{v}=0 \tag{2.16}$$

and

$$\boldsymbol{\tau}\cdot\hat{\boldsymbol{n}}=\alpha\,\boldsymbol{\sigma}\cdot\hat{\boldsymbol{n}}, \tag{2.17}$$

respectively. Here, $\hat{\boldsymbol{n}}$ is the outward unit normal from the deformed surface defined by $\hat{\boldsymbol{n}}=(\boldsymbol{\nabla}S/|\boldsymbol{\nabla}S|)$, where $S=\xi-1-f(\theta,\phi)$. The stress boundary condition in terms of different stress components is given by

$$\tau_{rr}-\frac{\tau_{r\theta}}{\xi}\frac{\partial f}{\partial\theta}-\frac{\tau_{r\phi}}{\xi\sin\theta}\frac{\partial f}{\partial\phi}=\alpha\left[\sigma_{rr}-\frac{\sigma_{r\theta}}{\xi}\frac{\partial f}{\partial\theta}-\frac{\sigma_{r\phi}}{\xi\sin\theta}\frac{\partial f}{\partial\phi}\right], \tag{2.18}$$

$$\tau_{r\theta}-\frac{\tau_{\theta\theta}}{\xi}\frac{\partial f}{\partial\theta}-\frac{\tau_{\theta\phi}}{\xi\sin\theta}\frac{\partial f}{\partial\phi}=\alpha\left[\sigma_{r\theta}-\frac{\sigma_{\theta\theta}}{\xi}\frac{\partial f}{\partial\theta}-\frac{\sigma_{\theta\phi}}{\xi\sin\theta}\frac{\partial f}{\partial\phi}\right] \tag{2.19}$$

and

$$\tau_{r\phi}-\frac{\tau_{\theta\phi}}{\xi}\frac{\partial f}{\partial\theta}-\frac{\tau_{\phi\phi}}{\xi\sin\theta}\frac{\partial f}{\partial\phi}=\alpha\left[\sigma_{r\phi}-\frac{\sigma_{\theta\phi}}{\xi}\frac{\partial f}{\partial\theta}-\frac{\sigma_{\phi\phi}}{\xi\sin\theta}\frac{\partial f}{\partial\phi}\right]. \tag{2.20}$$

Here, the τ_{ij} and σ_{ij} with $i,\,j=r,\,\theta,\,\phi$ are the components of the solid and fluid stress tensors, respectively. The boundary conditions are shifted onto the undeformed surface using the domain perturbation method (Leal 2007). In this method, we first performed the Taylor series expansion of the boundary conditions (2.16)–(2.20) about $\xi=1$. The regular asymptotic expansion of the variables in the problem ($\boldsymbol{v}$, $\boldsymbol{\sigma}$, p, $\boldsymbol{u}$, f, $\boldsymbol{\tau}$, ρ_p, $\boldsymbol{F}$, $\boldsymbol{T}$) are

https://doi.org/10.1017/jfm.2025.10754 Published online by Cambridge University Press

then substituted into these expanded boundary conditions. The regular expansions of the variables as series in α are given by

$$\boldsymbol{v} = \boldsymbol{v}^{(0)} + \alpha \boldsymbol{v}^{(1)} + \alpha^2 \boldsymbol{v}^{(2)} + \ldots, \tag{2.21}$$

$$\boldsymbol{\sigma} = \boldsymbol{\sigma}^{(0)} + \alpha \boldsymbol{\sigma}^{(1)} + \alpha^2 \boldsymbol{\sigma}^{(2)} + \ldots, \tag{2.22}$$

$$p = p^{(0)} + \alpha p^{(1)} + \alpha^2 p^{(2)} + \ldots, \tag{2.23}$$

$$\boldsymbol{u} = \alpha \boldsymbol{u}^{(1)} + \alpha^2 \boldsymbol{u}^{(2)} + \ldots, \tag{2.24}$$

$$f = \alpha f^{(1)} + \alpha^2 f^{(2)} + \ldots, \tag{2.25}$$

$$\boldsymbol{\tau} = \alpha \boldsymbol{\tau}^{(1)} + \alpha^2 \boldsymbol{\tau}^{(2)} + \ldots, \tag{2.26}$$

$$\rho_p = \rho_p^{(0)} + \alpha \rho_p^{(1)} + \alpha^2 \rho_p^{(2)} + \ldots, \tag{2.27}$$

$$\boldsymbol{F} = \boldsymbol{F}^{(0)} + \alpha \boldsymbol{F}^{(1)} + \alpha^2 \boldsymbol{F}^{(2)} + \ldots \tag{2.28}$$

and

$$\boldsymbol{T} = \boldsymbol{T}^{(0)} + \alpha \boldsymbol{T}^{(1)} + \alpha^2 \boldsymbol{T}^{(2)} + \ldots. \tag{2.29}$$

Note that the leading-order term in the series for the displacement field (2.24), the deformation (2.25) and the solid stress (2.26) arising from the deformation are $O(\alpha)$.

2.3.1. *Modified velocity boundary condition on the undeformed surface ($\xi = 1$)*
We have performed Taylor expansion of (2.16) about the undeformed surface ($\xi = 1$), and substituted the velocity and deformation expansions from (2.21) and (2.25), respectively, to obtain the modified velocity boundary conditions at various orders in α. At leading order, the boundary conditions are given by

$$\begin{aligned} \boldsymbol{v}^{(0)} &= 0 \quad \text{as } \xi = 1, \\ &\to -1\hat{\boldsymbol{k}} \quad \text{as } \xi \to \infty. \end{aligned} \tag{2.30}$$

At $O(\alpha)$, it is

$$\boldsymbol{v}^{(1)} + f^{(1)} \frac{\partial \boldsymbol{v}^{(0)}}{\partial \xi} = 0 \tag{2.31}$$

and at $O(\alpha^2)$, it is

$$\boldsymbol{v}^{(2)} + f^{(1)} \frac{\partial \boldsymbol{v}^{(1)}}{\partial \xi} + f^{(2)} \frac{\partial \boldsymbol{v}^{(0)}}{\partial \xi} + \frac{\left[f^{(1)}\right]^2}{2} \frac{\partial^2 \boldsymbol{v}^{(0)}}{\partial \xi^2} = 0. \tag{2.32}$$

Further, the velocity fields $\boldsymbol{v}^{(1)}$ and $\boldsymbol{v}^{(2)}$ decay as $\xi \to \infty$. Note that the boundary conditions in (2.31) and (2.32) are nonlinear. Although the governing equations are linear, the nonlinearity arises from applying the boundary conditions at the deformed surface whose shape is a part of the solution.

2.3.2. *Modified stress boundary conditions on the undeformed surface ($\xi = 1$)*
We have performed Taylor expansion of (2.17) about the undeformed surface ($\xi = 1$) and substituted the fluid stress, deformation and solid stress expansions from (2.22), (2.25) and (2.26), respectively, to obtain the modified stress boundary conditions at various orders in α.

https://doi.org/10.1017/jfm.2025.10754 Published online by Cambridge University Press

At $O(\alpha)$, the stress boundary conditions are

$$\tau_{rr}^{(1)} = \sigma_{rr}^{(0)}, \tag{2.33}$$

$$\tau_{r\theta}^{(1)} = \sigma_{r\theta}^{(0)}, \tag{2.34}$$

$$\tau_{r\phi}^{(1)} = \sigma_{r\phi}^{(0)}. \tag{2.35}$$

At $O(\alpha^2)$, they are

$$\tau_{rr}^{(2)} = \sigma_{rr}^{(1)} + f^{(1)}\frac{\partial}{\partial\xi}\left[\sigma_{rr}^{(0)} - \tau_{rr}^{(1)}\right], \tag{2.36}$$

$$\tau_{r\theta}^{(2)} = \sigma_{r\theta}^{(1)} - f^{(1)}\frac{\partial}{\partial\xi}\left[\tau_{r\theta}^{(1)} - \sigma_{r\theta}^{(0)}\right] + \frac{\partial f^{(1)}}{\partial\theta}\left[\tau_{\theta\theta}^{(1)} - \sigma_{\theta\theta}^{(0)}\right] + \frac{1}{\sin\theta}\frac{\partial f^{(1)}}{\partial\phi}\left[\tau_{\theta\phi}^{(1)} - \sigma_{\theta\phi}^{(0)}\right], \tag{2.37}$$

$$\tau_{r\phi}^{(2)} = \sigma_{r\phi}^{(1)} - f^{(1)}\frac{\partial}{\partial\xi}\left[\tau_{r\phi}^{(1)} - \sigma_{r\phi}^{(0)}\right] + \frac{\partial f^{(1)}}{\partial\theta}\left[\tau_{\theta\phi}^{(1)} - \sigma_{\theta\phi}^{(0)}\right] + \frac{1}{\sin\theta}\frac{\partial f^{(1)}}{\partial\phi}\left[\tau_{\phi\phi}^{(1)} - \sigma_{\phi\phi}^{(0)}\right], \tag{2.38}$$

and at $O(\alpha^3)$, they are

$$\begin{aligned}\tau_{rr}^{(3)} = {} & \sigma_{rr}^{(2)} - f^{(1)}\frac{\partial}{\partial\xi}\left[\tau_{rr}^{(2)} - \sigma_{rr}^{(1)}\right] - f^{(2)}\frac{\partial}{\partial\xi}\left[\tau_{rr}^{(1)} - \sigma_{rr}^{(0)}\right] - \frac{\left[f^{(1)}\right]^2}{2}\frac{\partial^2}{\partial\xi^2}\left[\tau_{rr}^{(1)} - \sigma_{rr}^{(0)}\right] \\ & + \frac{\partial f^{(2)}}{\partial\theta}\left[\tau_{r\theta}^{(1)} - \sigma_{r\theta}^{(0)}\right] + \frac{\partial f^{(1)}}{\partial\theta}\left[\tau_{r\theta}^{(2)} - \sigma_{r\theta}^{(1)}\right] + f^{(1)}\frac{\partial f^{(1)}}{\partial\theta}\frac{\partial}{\partial\xi}\left[\tau_{r\theta}^{(1)} - \sigma_{r\theta}^{(0)}\right] \\ & + \frac{1}{\sin\theta}\left(\frac{\partial f^{(2)}}{\partial\phi}\left[\tau_{r\phi}^{(1)} - \sigma_{r\phi}^{(0)}\right] + \frac{\partial f^{(1)}}{\partial\phi}\left[\tau_{r\phi}^{(2)} - \sigma_{r\phi}^{(1)}\right] + f^{(1)}\frac{\partial f^{(1)}}{\partial\phi}\frac{\partial}{\partial\xi}\left[\tau_{r\phi}^{(1)} - \sigma_{r\phi}^{(0)}\right]\right) \\ & - f^{(1)}\frac{\partial f^{(1)}}{\partial\theta}\left[\tau_{r\theta}^{(1)} - \sigma_{r\theta}^{(0)}\right] - \frac{1}{\sin\theta}\left(f^{(1)}\frac{\partial f^{(1)}}{\partial\phi}\left[\tau_{r\phi}^{(1)} - \sigma_{r\phi}^{(0)}\right]\right),\end{aligned} \tag{2.39}$$

$$\begin{aligned}\tau_{r\theta}^{(3)} = {} & \sigma_{r\theta}^{(2)} - f^{(1)}\frac{\partial}{\partial\xi}\left[\tau_{r\theta}^{(2)} - \sigma_{r\theta}^{(1)}\right] - f^{(2)}\frac{\partial}{\partial\xi}\left[\tau_{r\theta}^{(1)} - \sigma_{r\theta}^{(0)}\right] - \frac{\left[f^{(1)}\right]^2}{2}\frac{\partial^2}{\partial\xi^2}\left[\tau_{r\theta}^{(1)} - \sigma_{r\theta}^{(0)}\right] \\ & + \frac{\partial f^{(2)}}{\partial\theta}\left[\tau_{\theta\theta}^{(1)} - \sigma_{\theta\theta}^{(0)}\right] + \frac{\partial f^{(1)}}{\partial\theta}\left[\tau_{\theta\theta}^{(2)} - \sigma_{\theta\theta}^{(1)}\right] + f^{(1)}\frac{\partial f^{(1)}}{\partial\theta}\frac{\partial}{\partial\xi}\left[\tau_{\theta\theta}^{(1)} - \sigma_{\theta\theta}^{(0)}\right] \\ & + \frac{1}{\sin\theta}\left(\frac{\partial f^{(2)}}{\partial\phi}\left[\tau_{\theta\phi}^{(1)} - \sigma_{\theta\phi}^{(0)}\right] + \frac{\partial f^{(1)}}{\partial\phi}\left[\tau_{\theta\phi}^{(2)} - \sigma_{\theta\phi}^{(1)}\right] + f^{(1)}\frac{\partial f^{(1)}}{\partial\phi}\frac{\partial}{\partial\xi}\left[\tau_{\theta\phi}^{(1)} - \sigma_{\theta\phi}^{(0)}\right]\right) \\ & - f^{(1)}\frac{\partial f^{(1)}}{\partial\theta}\left[\tau_{\theta\theta}^{(1)} - \sigma_{\theta\theta}^{(0)}\right] - \frac{1}{\sin\theta}\left(f^{(1)}\frac{\partial f^{(1)}}{\partial\phi}\left[\tau_{\theta\phi}^{(1)} - \sigma_{\theta\phi}^{(0)}\right]\right),\end{aligned} \tag{2.40}$$

$$\begin{aligned}\tau_{r\phi}^{(3)} = {} & \sigma_{r\phi}^{(2)} - f^{(1)}\frac{\partial}{\partial\xi}\left[\tau_{r\phi}^{(2)} - \sigma_{r\phi}^{(1)}\right] - f^{(2)}\frac{\partial}{\partial\xi}\left[\tau_{r\phi}^{(1)} - \sigma_{r\phi}^{(0)}\right] - \frac{\left[f^{(1)}\right]^2}{2}\frac{\partial^2}{\partial\xi^2}\left[\tau_{r\phi}^{(1)} - \sigma_{r\phi}^{(0)}\right] \\ & + \frac{\partial f^{(2)}}{\partial\theta}\left[\tau_{\theta\phi}^{(1)} - \sigma_{\theta\phi}^{(0)}\right] + \frac{\partial f^{(1)}}{\partial\theta}\left[\tau_{\theta\phi}^{(2)} - \sigma_{\theta\phi}^{(1)}\right] + f^{(1)}\frac{\partial f^{(1)}}{\partial\theta}\frac{\partial}{\partial\xi}\left[\tau_{\theta\phi}^{(1)} - \sigma_{\theta\phi}^{(0)}\right]\end{aligned}$$

https://doi.org/10.1017/jfm.2025.10754 Published online by Cambridge University Press

$$+\frac{1}{\sin\theta}\left(\frac{\partial f^{(2)}}{\partial\phi}\left[\tau^{(1)}_{\phi\phi}-\sigma^{(0)}_{\phi\phi}\right]+\frac{\partial f^{(1)}}{\partial\phi}\left[\tau^{(2)}_{\phi\phi}-\sigma^{(1)}_{\phi\phi}\right]+f^{(1)}\frac{\partial f^{(1)}}{\partial\phi}\frac{\partial}{\partial\xi}\left[\tau^{(1)}_{\phi\phi}-\sigma^{(0)}_{\phi\phi}\right]\right)$$
$$-f^{(1)}\frac{\partial f^{(1)}}{\partial\theta}\left[\tau^{(1)}_{\theta\phi}-\sigma^{(0)}_{\theta\phi}\right]-\frac{1}{\sin\theta}\left(f^{(1)}\frac{\partial f^{(1)}}{\partial\phi}\left[\tau^{(1)}_{\phi\phi}-\sigma^{(0)}_{\phi\phi}\right]\right). \tag{2.41}$$

The deformation of the surface at different orders $f^{(1)}$ and $f^{(2)}$ appearing in the modified boundary conditions are obtained by expanding (2.8) using a Taylor series about $\xi=1$ and substituting (2.24) and (2.25). At $O(\alpha)$, $f^{(1)}$ is given by

$$f^{(1)}=u^{(1)}_r\Big|_{\xi=1}. \tag{2.42}$$

At $O(\alpha^2)$, $f^{(2)}$ is given by

$$f^{(2)}=\left(u^{(2)}_r+f^{(1)}\frac{\partial u^{(1)}_r}{\partial\xi}-\frac{\left[u^{(1)}_\theta\right]^2+\left[u^{(1)}_\phi\right]^2}{2}\right)\Bigg|_{\xi=1}. \tag{2.43}$$

The modified boundary conditions, together with the series solutions described in the previous sections, are used to calculate all the variables defined in (2.21)–(2.29) in the unbounded domain.

2.4. *Method of reflections*

To capture the effect of the wall on the dynamics of the translating particle, we have employed the method of reflections (Kim & Karrila 2013). The unbounded velocity field ($\boldsymbol{v}_{un}$) does not satisfy the no-slip boundary condition at the wall (see figure 1*c*). The velocity field is alternatively reflected from the wall ($\boldsymbol{v}_{w_k}$) and the sphere ($\boldsymbol{v}_{s_k}$), and the reflected fields are added to the unbounded velocity field to satisfy the boundary conditions at both the surfaces to the desired accuracy. The desired accuracy can be quantified in algebraic powers of $1/H$. Therefore, the reflected velocity fields are expanded as series in $1/H$. The total velocity field at each order in α^n ($n=0,\,1,\,2\ldots$) is written as

$$\boldsymbol{v}^{(n)}=\boldsymbol{v}^{(n)}_{un}+\frac{\boldsymbol{v}^{(n,H)}_{w_1}}{H}+\frac{\boldsymbol{v}^{(n,H^2)}_{w_1}}{H^2}+\ldots+\frac{\boldsymbol{v}^{(n,H)}_{s_1}}{H}+\frac{\boldsymbol{v}^{(n,H^2)}_{w_2}}{H^2}+\frac{\boldsymbol{v}^{(n,H^3)}_{w_2}}{H^3}+\ldots+\frac{\boldsymbol{v}^{(n,H^2)}_{s_2}}{H^2}$$
$$+\frac{\boldsymbol{v}^{(n,H^3)}_{w_3}}{H^3}+\frac{\boldsymbol{v}^{(n,H^4)}_{w_3}}{H^4}+\ldots+\frac{\boldsymbol{v}^{(n,H^3)}_{s_3}}{H^3}+\frac{\boldsymbol{v}^{(n,H^4)}_{w_4}}{H^4}+\ldots. \tag{2.44}$$

Here, the subscripts $()_{un}$ and $()_{w_k}$ denote the unbounded field and the k^{th} reflected field from the wall, respectively. The subscript $()_{s_k}$ indicates that the velocity field includes the effect of the k^{th} reflection from the sphere. The superscript $(n,\,H^p)$ indicates the $1/H^p$ term in the series at $O(\alpha^n)$. Similar to the velocity field, the fluid stress $\boldsymbol{\sigma}^{(n)}$ and pressure $p^{(n)}$ are also expanded as a series in $1/H$. The displacement $\boldsymbol{u}^{(n)}$ at each order in $\alpha^n(n=1,\,2,\ldots)$ is expanded as a series in $1/H$ as

$$\boldsymbol{u}^{(n)}=\boldsymbol{u}^{(n)}_{un}+\frac{\boldsymbol{u}^{(n,H)}_{s_1}}{H}+\frac{\boldsymbol{u}^{(n,H^2)}_{s_2}}{H^2}+\frac{\boldsymbol{u}^{(n,H^3)}_{s_3}}{H^3}+\ldots. \tag{2.45}$$

Similar to the displacement field, the solid stress $\boldsymbol{\tau}^{(n)}$, deformation $f^{(n)}$, point force $\boldsymbol{F}^{(n)}$ and point torque $\boldsymbol{T}^{(n)}$ are expanded as a series in $1/H$. We have derived the results until $\mathrm{O}(1/H^3)$, which needs three reflections from the wall in the first case where

https://doi.org/10.1017/jfm.2025.10754 Published online by Cambridge University Press

gravity is aligned with the particle velocity. In the second case where gravity is in an arbitrary direction, the results are derived until $O(1/H^2)$, which needs two reflections from the wall.

2.5. *Solution procedure*

Here, we describe the steps involved in calculating the point force and the point torque required to make the particle translate parallel to the wall. Steps (i)–(iv) are for an unbounded domain, and steps (v)–(ix) are for capturing the wall effects using the method of reflections.

(i) First, we calculated the fields $(\boldsymbol{v}_{un}^{(0)}, p_{un}^{(0)})$ surrounding the particle in an unbounded domain. At $O(1)$, the constants in (2.9)–(2.11) are determined by applying the velocity boundary condition in (2.30) and the corresponding fluid stress field $\boldsymbol{\sigma}_{un}^{(0)}$ is calculated.

(ii) Using stress continuity in (2.33)–(2.35), $\boldsymbol{\tau}_{un}^{(1)}$, $\boldsymbol{u}_{un}^{(1)}$, $\boldsymbol{F}_{un}^{(0)}$, $\boldsymbol{T}_{un}^{(0)}$ and $f_{un}^{(1)}$ are calculated.

(iii) We then use (2.31) to determine $\boldsymbol{v}_{un}^{(1)}$ and in turn calculate $\boldsymbol{\sigma}_{un}^{(1)}$.

(iv) Steps (ii) and (iii) are repeated at the next orders in α to determine the velocity and the stress fields in the fluid, the external forces and the external torques until $O(\alpha^2)$, and the displacement and stress fields in the solid until $O(\alpha^3)$.

(v) To capture the wall effects, the unbounded velocity and pressure fields until $O(\alpha^2)$ are reflected from the wall, to determine the first wall-reflected fields at various orders given by $[(\boldsymbol{v}_{w_1}^{(0,H)}/H) + \alpha(\boldsymbol{v}_{w_1}^{(1,H)}/H) + \alpha^2(\boldsymbol{v}_{w_1}^{(2,H)}/H)]$, $[(\boldsymbol{v}_{w_1}^{(0,H^2)}/H^2) + \alpha(\boldsymbol{v}_{w_1}^{(1,H^2)}/H^2)]$ and $\boldsymbol{v}_{w_1}^{(0,H^3)}/H^3$.

(vi) The velocity fields $\boldsymbol{v}_{w_1}^{(n,H)}$(with $n = 0,1,2$) are reflected from the sphere to determine the first sphere-reflected fields given by $[(\boldsymbol{v}_{s_1}^{(0,H)}/H) + \alpha(\boldsymbol{v}_{s_1}^{(1,H)}/H) + \alpha^2(\boldsymbol{v}_{s_1}^{(2,H)}/H)]$ and the displacement fields given by $[\alpha(\boldsymbol{u}_{s_1}^{(1,H)}/H) + \alpha^2(\boldsymbol{u}_{s_1}^{(2,H)}/H)]$ using the boundary conditions at the sphere surface. We followed the same steps as those described for the unbounded domain to calculate the higher-order term in α.

(vii) The velocity fields $\boldsymbol{v}_{s_1}^{(n,H)}$ (with $n = 0,1$) are reflected from the wall to determine the second wall-reflected fields given by $[(\boldsymbol{v}_{w_2}^{(0,H^2)}/H^2) + \alpha(\boldsymbol{v}_{w_2}^{(1,H^2)}/H^2)]$ and $\boldsymbol{v}_{w_2}^{(0,H^3)}/H^3$. All the $O(1/H^2)$ terms from the first and second wall reflections are used to determine the second sphere-reflected fields given by $[(\boldsymbol{v}_{s_2}^{(0,H^2)}/H^2) + \alpha(\boldsymbol{v}_{s_2}^{(1,H^2)}/H^2)]$ and the displacement field given by $[\alpha(\boldsymbol{u}_{s_2}^{(1,H^2)}/H^2)]$ using the boundary conditions at the sphere surface.

(viii) The velocity field $\boldsymbol{v}_{s_2}^{(0,H^2)}$ is reflected from the wall to determine the third wall-reflected field given by $(\boldsymbol{v}_{w_3}^{(0,H^3)}/H^3)$. All the $O(1/H^3)$ terms in the first three wall reflections are used to calculate the third sphere-reflected field given by $\boldsymbol{v}_{s_3}^{(0,H^3)}/H^3$.

(ix) At each of the reflections from the sphere, we also determine the point force and the point torque at different orders.

https://doi.org/10.1017/jfm.2025.10754 Published online by Cambridge University Press

3. Results

Here, we discuss the results of our analysis. The discussion is presented for two cases: (i) gravity aligned with the particle velocity in § 3.1 and (ii) gravity in an arbitrary direction in § 3.2.

3.1. *Gravity aligned with particle velocity*

First, we discuss the results for the case of translation of the particle along the direction of gravity ($\boldsymbol{g} = g_z\hat{\boldsymbol{k}}$) in an unbounded domain. The leading-order velocity field $[\boldsymbol{v}_{un}^{(0)}]$ is obtained by applying (2.30) to determine the constants in the series solution in § 2.1. The field is the same as that in a uniform flow past a rigid sphere of radius R_0 in an unbounded domain (Guazzelli & Morris 2011). The stress field at $O(\alpha)$ in the solid is calculated using the boundary conditions (2.33)–(2.35), and the corresponding displacement components are obtained as

$$u_{un,r}^{(1)} = \frac{1}{\xi}C_1\cos\theta + \xi^2 C_2\cos\theta, \tag{3.1}$$

$$u_{un,\theta}^{(1)} = \frac{1}{\xi}\left[-\frac{3+\gamma}{4+2\gamma}C_1\right]\sin\theta + \xi^2\left[\frac{(3+2\gamma)(2K_{fz}-9(1+\gamma))-K_{fz}\gamma\tilde{\rho}}{(-1+\gamma)(9-2K_{fz}+9\gamma)+K_{fz}(4+5\gamma)\tilde{\rho}}C_2\right]\sin\theta. \tag{3.2}$$

Here,

$$C_1 = \frac{1}{6}\left(9-2K_{fz}(-1+\tilde{\rho})\right),$$
$$C_2 = -\frac{-9+9\gamma^2+K_{fz}(2+4\tilde{\rho}+\gamma(-2+5\tilde{\rho}))}{6(2+\gamma)(2+3\gamma)}. \tag{3.3}$$

Additionally, $\tilde{\rho} = \rho_p^{(0)}/\rho_f$ and $K_{fz} = \rho_f R_0^2 g_z/(\mu V_0)$, the ratio of gravitational to the viscous forces. The surface deformation $f_{un}^{(1)}$ is calculated from (2.42) and is obtained as

$$f_{un}^{(1)} = C_3\cos\theta, \tag{3.4}$$

where $C_3 = C_1 + C_2$. Using the boundary condition (2.31), the velocity components and pressure in the fluid at $O(\alpha)$ are obtained as

$$v_{un,r}^{(1)} = \left[\frac{1}{\xi^2}-\frac{1}{\xi^4}\right]\frac{3\,C_3}{4}(3\cos^2\theta-1), \tag{3.5}$$

$$v_{un,\theta}^{(1)} = -\frac{1}{\xi^4}\left[\frac{3\,C_3}{2}\right]\cos\theta\sin\theta, \tag{3.6}$$

$$v_{un,\phi}^{(1)} = 0, \tag{3.7}$$

$$p_{un}^{(1)} = \frac{1}{\xi^3}\left[\frac{3\,C_3}{2}\right](3\cos^2\theta-1). \tag{3.8}$$

The stress field in the solid at $O(\alpha^2)$ is calculated using the boundary conditions (2.36)–(2.38) and the corresponding displacement components are obtained as

$$u_{un,r}^{(2)} = \xi\left[A_1 + A_2\cos^2\theta\right] + \xi^3 A_3\left(1-3\cos^2\theta\right), \tag{3.9}$$

$$u_{un,\theta}^{(2)} = -\xi A_2\cos\theta\sin\theta + \xi^3\left[\frac{(7+5\gamma)}{\gamma}A_3\right]\sin\theta\cos\theta. \tag{3.10}$$

https://doi.org/10.1017/jfm.2025.10754 Published online by Cambridge University Press

Here,

$$A_1 = \left[\frac{-168+\gamma(-48+3\gamma(152+97\gamma)-2K_{fz}(48+\gamma(98+45\gamma))(-1+\tilde{\rho}))}{4(2+\gamma)(2+3\gamma)(14+19\gamma)}\right]C_3,$$
$$A_2 = \left[\frac{-336-3\gamma(214+97\gamma)+2K_{fz}(4+5\gamma)(14+9\gamma)(-1+\tilde{\rho})}{4(2+\gamma)(14+19\gamma)}\right]C_3,$$
$$A_3 = \left[\frac{2\gamma(1+\gamma)(-9+2K_{fz}(-1+\tilde{\rho}))}{(2+\gamma)(14+19\gamma)}\right]C_3. \tag{3.11}$$

The surface deformation $f_{un}^{(2)}$ is calculated from (2.43) and is obtained as

$$f_{un}^{(2)} = D_1 + D_2\cos^2\theta - \frac{1}{2}D_3^2\sin^2\theta. \tag{3.12}$$

Here,

$$D_1 = A_1 + A_3,$$
$$D_2 = A_2 - 3A_3 - C_3(-3C_2 + C_3),$$
$$D_3 = \frac{(C_2-C_3)(3+\gamma)}{2(2+\gamma)} + \frac{C_2\left((3+2\gamma)(2K_{fz}-9(1+\gamma))-K_{fz}\gamma\tilde{\rho}\right)}{(-1+\gamma)(9-2K_{fz}+9\gamma)+K_{fz}(4+5\gamma)\tilde{\rho}}. \tag{3.13}$$

Using (2.32), we calculated $\boldsymbol{v}_{un}^{(2)}$ and then derived the stress field $\boldsymbol{\tau}_{un}^{(3)}$ using the boundary conditions (2.39)–(2.41). The expressions for components of $\boldsymbol{v}_{un}^{(2)}$ are provided in (B1) and (B2) of Appendix B. The point force until $O(\alpha^2)$ in dimensional form is obtained as

$$\boldsymbol{F}_{un} = 6\pi\mu V_0 R_0\left(\left[1+\frac{2K_{fz}}{9}(1-\tilde{\rho})\right] + \alpha^2\left[E_1 + K_{fz}^3(E_2I_1) + K_{fz}^2(E_2E_3I_2) + K_{fz}(E_4E_2I_3)\right]\right)\hat{\boldsymbol{k}}\,. \tag{3.14}$$

The expressions for E_1, E_2, E_3, E_4, I_1, I_2 and I_3 in the equation are given in (B3)–(B7) of Appendix B. The leading order force in the equation reduces to the sum of Stokes drag and the buoyancy force on a rigid sphere. The particle should not experience a hydrodynamic lift force or a torque due to the symmetry of the flow field about the z-axis in the unbounded domain. Consistently, the point force at $O(\alpha^2)$ in the equation acts only along gravity (z-axis) and the point torque is also zero. The point force at $O(\alpha^2)$ balances the hydrodynamic forces arising from the change in the particle shape and the buoyancy force. The change in the buoyancy force at $O(\alpha^2)$ arises from compressibility-induced variations in the particle's volume and density.

To analyse the shape of the deformed particle, we have plotted it on the $y=0$ plane, as shown in figure 2(a). As is evident in the figure, the shape is symmetric about the z-axis. The dip at the top is due to the effect of the point force applied at the centre of the particle. The shape we obtain differs from that obtained by Murata (1980), also shown in the figure. Murata calculated the velocity of a weakly elastic spherical particle sedimenting due to gravity. He showed that the particle deforms to a prolate spheroid. The shape difference between ours and Murata's work arises from the varying force distributions: our problem considers equilibrium between external, gravitational and hydrodynamic forces, whereas Murata's formulation considers only gravitational and hydrodynamic forces. Consequently, the hydrodynamic forces acting on the particle differ between the two problems. Additionally, our approach accounts for the density change due to the

https://doi.org/10.1017/jfm.2025.10754 Published online by Cambridge University Press

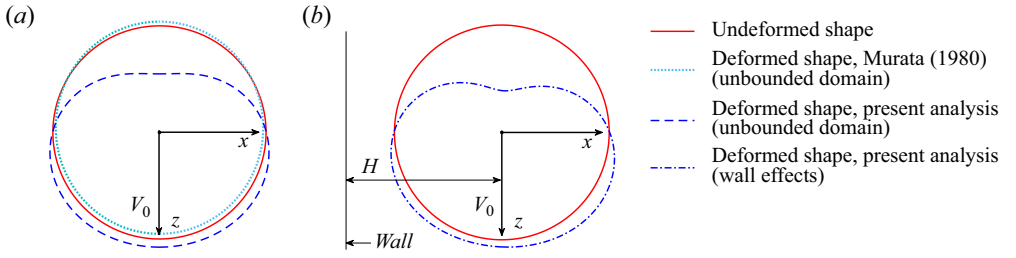


Figure 2. Shape of the deformed sphere on the xz-plane at $\alpha = 0.2$, $\tilde{\rho} = 1.05$, $K_{fz} = 0.5$ and $\gamma = 2$ in the (a) unbounded domain and (b) presence of wall at $H = 2.5$.

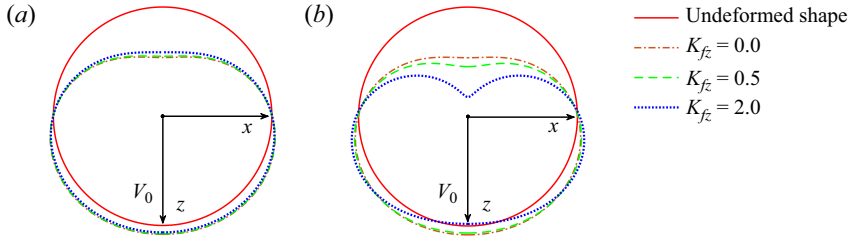


Figure 3. Variation in the shape of the deformed sphere in the unbounded domain as a function of K_{fz} at $\gamma = 2$, $\alpha = 0.2$ when (a) the particle is denser than the fluid, $\tilde{\rho} = 1.05$ and (b) the particle is lighter than the fluid, $\tilde{\rho} = 0.05$.

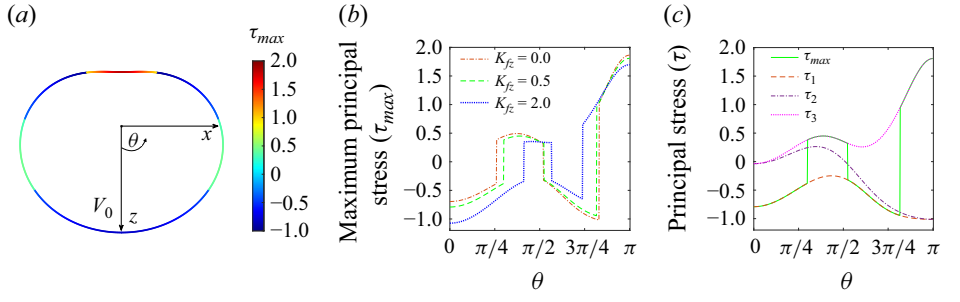


Figure 4. Variation of the maximum principal stress (based on its absolute value) along the particle surface in the unbounded domain (a) for $K_{fz} = 0.5$ and (b) for different values of K_{fz}. (c) Variation of the principal stresses (τ_1, τ_2 and τ_3) and τ_{max} for $K_{fz} = 0.5$, along the particle surface, plotted at $\gamma = 2$, $\alpha = 0.2$ and $\tilde{\rho} = 1.05$ for θ varying from 0 to π.

compressibility of the particle, an aspect not considered in Murata's calculation for the terminal velocity, although he models the particle as a compressible one.

The deformed shape of the particle depends on the ratio of the particle density to the ambient fluid ($\tilde{\rho}$). For a particle heavier than the surrounding fluid, as K_{fz} (defined as $\rho_f R_0^2 g_z/(\mu V_0)$ following (2.12)) increases, the external force required to balance hydrodynamic drag diminishes, resulting in a reduction in the dip in the particle's upper section as shown in figure 3(a). Conversely, for a particle lighter than the ambient fluid, an increase in K_{fz} necessitates a larger external force to sustain translation, which in turn enhances the dip in the particle's upper section as shown in figure 3(b). Figure 4(a) illustrates the variation of the maximum principal stress (based on its absolute value), denoted by τ_{max}, along the surface of a heavier particle for $K_{fz} = 0.5$. In figure 4(b), τ_{max}

https://doi.org/10.1017/jfm.2025.10754 Published online by Cambridge University Press

is plotted against θ for different values of K_{fz}. The maximum principal stress is tensile in nature near $\theta = \pi$, the location of the dip in the deformed shape. As K_{fz} increases, the point force diminishes, leading to a reduction in the maximum principal stress near $\theta = \pi$. This trend aligns with the less pronounced dip seen in figure 3(*a*). The observed jumps in figure 4(*b*) occur at locations where the nature of the maximum principal stress changes, from compressive to tensile or *vice versa* for different values of K_{fz}. To see the jumps, we have plotted the variation of principal stresses (τ_1, τ_2 and τ_3) and τ_{max} against θ, corresponding to $K_{fz} = 0.5$ along the particle surface in figure 4(*c*), as θ varies from 0 to π. As is evident from the figure, the principal stresses remain continuous, whereas discontinuities (jumps) appear in the plot of τ_{max} due to the use of the true value of maximum absolute principal stress. Due to the applied point force at the origin, the lower-most surface of the particle experiences compressive stress, while the upper-most surface is under tensile stress. Along the surface, the stress undergoes transition from compressive to tensile, then tensile to compressive and finally from compressive back to tensile, as θ varies from 0 to π.

Now, we discuss the case of the particle translating next to a wall. In the presence of the wall, the calculations are carried out using the method of reflections described in § 2.4. The velocity and displacement fields are calculated at orders $1/H$, α/H, α^2/H, $1/H^2$, α/H^2 and $1/H^3$. The surface deformation until the order considered is obtained as

$$f = f_{un} + \alpha\left[\frac{B_1\cos\theta}{H}\left(1+\frac{9}{16H}\right)+\frac{45\cos\phi\sin 2\theta}{64H^2}\right] + \alpha^2\left[\left(\frac{B_2}{H}+K_{fz}\frac{B_3}{H}\right)+\left(\frac{B_4}{H}+K_{fz}\frac{B_5}{H}\right)\cos 2\theta\right]. \tag{3.15}$$

The expressions for B_1, B_2, B_3, B_4 and B_5 in the equation are given in (B10)–(B13) of Appendix B. The deformation in the unbounded domain $f_{un} = \alpha f_{un}^{(1)} + \alpha^2 f_{un}^{(2)}$, where $f_{un}^{(1)}$ and $f_{un}^{(2)}$ are presented in (3.4) and (3.12), respectively. Due to the presence of the wall, the deformed shape is not symmetric about the z-axis and is a function of ϕ at $O(\alpha/H^2)$. This contrasts with the unbounded case, where the deformed shape remains independent of ϕ. We have plotted the shape of the particle in the xz- plane passing through the origin in figure 2(*b*) to illustrate the asymmetry. The dash-dotted curve is plotted using (2.7) and the shape is not symmetric about the z-axis.

The point force on the particle until the order considered is obtained as

$$\boldsymbol{F} = \boldsymbol{F}_{un} + 6\pi\mu V_0 R_0\left(\left[\frac{9}{16H}+\frac{81}{256H^2}+\frac{217}{4096H^3}\right]\hat{\boldsymbol{k}} - \frac{\alpha}{H^2}\left[\frac{9}{64}\right]\hat{\boldsymbol{i}} + \frac{\alpha^2}{H}\left[\frac{9E_1}{4}+K_{fz}^2E_2I_4+K_{fz}I_5\right]\hat{\boldsymbol{k}}\right). \tag{3.16}$$

The expressions for I_4 and I_5 are given in (B8) and (B9) of Appendix B. The point force due to wall effects at the leading order balances the buoyancy force and the hydrodynamic force, derived in the literature for the case of a rigid sphere (Faxen 1923; Goldman *et al.* 1967). It is important to note that the elastic effects lead to a hydrodynamic lift away from the wall, which is balanced by the point force at $O(\alpha/H^2)$ in the equation. Further, the wall effects also result in a correction to the drag at $O(\alpha^2/H)$ along the z-direction, leading to a point force at the same order in the equation. The point torque is zero until the order we have considered in our calculation. The force in (3.16) is presented until $O(1/H^3)$ assuming $\alpha = O(1/H)$. The assumption simplifies the analysis as the calculation becomes cumbersome if this scaling is not taken into account. For instance, the leading-order lift

https://doi.org/10.1017/jfm.2025.10754 Published online by Cambridge University Press

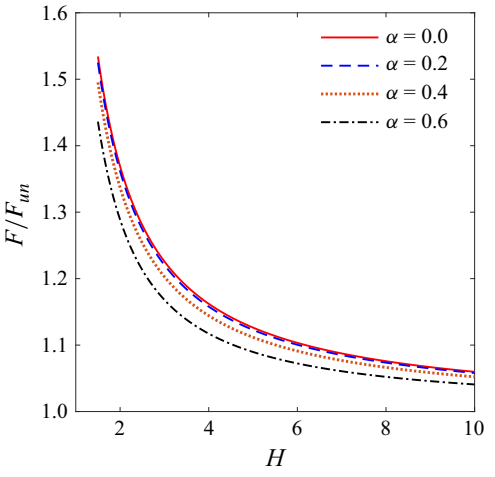


Figure 5. Variation of external point force (parallel to the wall) given in (3.16) relative to the unbounded given in (3.14) for different wall–particle gap widths, H varying from 1.5 to 10 at $\tilde{\rho} = 1.05$, $K_{fz} = 0.5$ and $\gamma = 2$.

comes at $O(\alpha/H^2)$. If $\alpha \gg O(1/H)$ and say $\alpha^3 = O(1/H)$, then to ensure consistency with the lift at leading order, the calculation has to be carried out to include the corrections at $O(\alpha^4/H)$ as well. For this, one needs to use the modified boundary conditions at the sphere surface (§ 2.3) at $O(\alpha^4)$ as well. Implementing the boundary conditions and performing the resulting calculations is cumbersome. Therefore, we assume $\alpha = O(1/H)$ to simplify the analysis.

Here, we discuss the scaling behaviour of the forces at different orders in α/H. In the unbounded domain, the drag force arising from particle deformation scales (at $O(\alpha^2)$) as $(\mu^3 V_0^3/G^2)(1/R_0)$. Due to the wall effects, the drag force due to the deformation at the leading-order scales (at $O(\alpha^2/H)$) as $(\mu^3 V_0^3/G^2)(1/h)$. The leading-order lift appears at $O(\alpha/H^2)$, which scales as $(\mu^2 V_0^2/G)(R_0/h)^2$. The scaling for the lift can be seen as arising from the stresslet velocity field (that decays as $1/\xi^2$, as seen in (3.5)). One can estimate the scaling of the stresslet singularity (S_t) as $(\mu V_0 R_0) \times (\mu V_0/G)$, the term in the first bracket being the viscous force scaling and that in the second is the scaling for the elastic deformation. The velocity field after reflecting from the wall scales as $S_t/(\mu h^2)$ and acts as an ambient for the elastic particle, which results in the force scaling given by $\mu[S_t/(\mu h^2)]R_0 = (\mu^2 V_0^2/G)(R_0/h)^2$. For an elastic sphere moving parallel to a rigid wall in the lubrication limit, the scaling in the lubrication limit is $(\mu^2 V_0^2/G)(R_0/h)^{5/2}$ (expressed using the variables adopted in our analysis) (Skotheim & Mahadevan 2005). Note that the decay rate of the lift force obtained in our calculation is different from that predicted in the lubrication limit.

Figure 5 shows the variation of F/F_{un}, the ratio of point forces in the semi-infinite and unbounded domain acting along z-axis, with H, for different values of α. The figure illustrates that the particle experiences greater resistance to the flow when it is near the wall than when it is away. Additionally, as the particle deformability increases, the force ratio decreases at a given H. The deformed shape of the particle at different values of γ for fixed H value at $\alpha = 0.2$ is shown in figure 6(*a*). As expected, particles with larger γ exhibit reduced volumetric deformation compared with those with lower γ. Figure 6(*b*) illustrates the variation of deformed shape with H at a constant γ. As H decreases, the particle experiences greater flow resistance and the asymmetry in the deformed shape increases.

https://doi.org/10.1017/jfm.2025.10754 Published online by Cambridge University Press

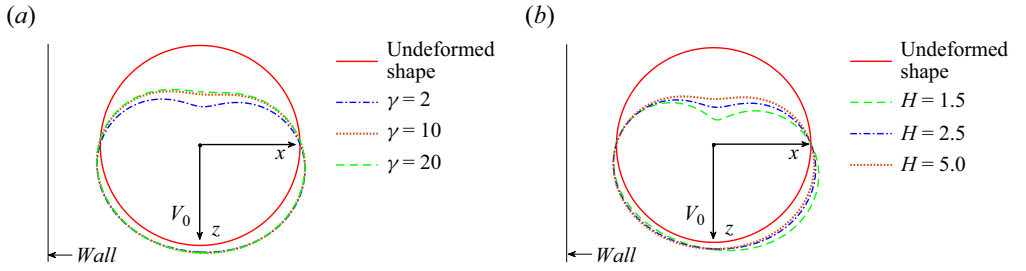


Figure 6. Variation in the shape of the deformed sphere on the xz-plane at $\alpha = 0.2$; (a) for different values of γ at $H = 2.5$ and (b) for different values of H at $\gamma = 2$.

The point force for a neutrally buoyant particle can be obtained by equating the particle and fluid densities at the leading order ($\tilde{\rho} = 1$, defined following (3.3)) in (3.16) and is obtained as

$$\boldsymbol{F}_{nb} = 6\pi\mu V_0 R_0 \left[\left(1 + \frac{9}{16H} + \frac{81}{256H^2} + \frac{217}{4096H^3} \right) \hat{\boldsymbol{k}} - \alpha \left(\frac{9}{64H^2} \right) \hat{\boldsymbol{i}} + \alpha^2 \left(E_1 \left[1 + \frac{9}{4H} \right] + K_{fz}^3 E_2 + K_{fz}^2 \left(E_3 - \frac{27(8 + 69\gamma + 10\gamma^2)}{160(2+\gamma)\, H} \right) E_2 + K_{fz} \left[E_4 E_2 + \frac{E_5}{H} \right] \right) \hat{\boldsymbol{k}} \right]. \tag{3.17}$$

Here,

$$E_5 = -\frac{9\left(1792 + 6354\gamma + 7213\gamma^2 + 2922\gamma^3 + 475\gamma^4\right)}{64(2+\gamma)(2+3\gamma)^2(14+19\gamma)}. \tag{3.18}$$

It is worth noting that even a neutrally buoyant particle experiences a buoyancy force at $O(\alpha^2)$ due to its compressibility. In the absence of gravity or when $K_{fz} \ll 1$, a limit relevant for microfluidic devices, (3.16) simplified further and one gets the force as

$$\boldsymbol{F}_{0g} = 6\pi\mu V_0 R_0 \left[\left(1 + \frac{9}{16H} + \frac{81}{256H^2} + \frac{217}{4096H^3} \right) \hat{\boldsymbol{k}} - \alpha \left(\frac{9}{64H^2} \right) \hat{\boldsymbol{i}} + \alpha^2 E_1 \left(1 + \frac{9}{4H} \right) \hat{\boldsymbol{k}} \right]. \tag{3.19}$$

3.2. *Gravity in an arbitrary direction*

Here, we present the point force and the point torque for the case of the particle translating parallel to the wall and gravity is in an arbitrary direction ($\boldsymbol{g} = g_x\hat{\boldsymbol{i}} + g_y\hat{\boldsymbol{j}} + g_z\hat{\boldsymbol{k}}$). Following the procedure outlined in § 2.5, we first calculated the variables in an unbounded domain and then accounted for wall effects using the method of reflections. Due to the misalignment between gravity and the particle velocity, the deformed shape of the particle lacks symmetry about the z-axis even in the unbounded domain. The point forces in unbounded and semi-infinite domains for arbitrary gravity are represented by $\boldsymbol{F}_{un,ag}$ and $\boldsymbol{F}_{ag}$, respectively. The force in the unbounded domain is obtained as

$$\boldsymbol{F}_{un,ag} = 6\pi\mu V_0 R_0 \left(\left[\left(1 + \frac{2K_{fz}}{9}\left[1 - \tilde{\rho}\right] \right) \hat{\boldsymbol{k}} + \frac{2[1-\tilde{\rho}]}{9} \left(K_{fx}\hat{\boldsymbol{i}} + K_{fy}\hat{\boldsymbol{j}} \right) \right] + \alpha^2 \left[F^{(2)}_{un,ag_x}\hat{\boldsymbol{i}} + F^{(2)}_{un,ag_y}\hat{\boldsymbol{j}} + F^{(2)}_{un,ag_z}\hat{\boldsymbol{k}} \right] \right). \tag{3.20}$$

https://doi.org/10.1017/jfm.2025.10754 Published online by Cambridge University Press

The Cartesian components of the force coefficient at $O(\alpha^2)$, denoted as $F^{(2)}_{un,ag_i}$ ($i = x, y, z$), are given in Appendix C. Note that the force at $O(\alpha^2)$ along the z-direction is a function of K_{fx}, K_{fy}, K_{fz}, γ and $\tilde{\rho}$, and is not the same as that at $O(\alpha^2)$ in (3.14), where it is only a function of K_{fz}, γ and $\tilde{\rho}$. Therefore, the body forces in the x- and y-directions also affect the force in the z-direction in the arbitrary gravity case, due to the nonlinearity in the boundary conditions. The drag at $O(\alpha^2)$ scales as $(\mu^3 V_0^3/G^2)(1/R_0)$. Further, the torque comes at $O(\alpha)$ and is obtained as

$$\boldsymbol{T}_{un,ag} = 8\pi\mu V_0 R_0^2 \left(\alpha \left[\frac{2-2\gamma(1-\tilde{\rho})+\tilde{\rho}}{8(2+3\gamma)}\left(-K_{fy}\hat{\boldsymbol{i}} + K_{fx}\hat{\boldsymbol{j}}\right)\right]\right). \tag{3.21}$$

Due to the elastic effects, the torque appears at $O(\alpha)$ in this case, while it is zero when gravity is aligned with the particle velocity. The torque at $O(\alpha)$ scales as $(\mu^2 V_0^2/G)(R_0)$.

The simplified form of the point force ($\boldsymbol{F}^x_{un,ag}$) and the point torque ($\boldsymbol{T}^x_{un,ag}$) when gravity acts along the x-axis ($\boldsymbol{g} = g_x\hat{\boldsymbol{i}}$) is obtained by substituting $K_{fy} = K_{fz} = 0$ in (3.20) and (3.21), respectively. The point force is obtained as

$$\boldsymbol{F}^x_{un,ag} = 6\pi\mu V_0 R_0 \left(\left[1\,\hat{\boldsymbol{k}} + \frac{2(1-\tilde{\rho})}{9}K_{fx}\hat{\boldsymbol{i}}\right] + \alpha^2\left[F^{(2),x}_{un,ag_x}\hat{\boldsymbol{i}} + F^{(2),x}_{un,ag_z}\hat{\boldsymbol{k}}\right]\right). \tag{3.22}$$

Here,

$$\begin{aligned}
F^{(2),x}_{un,ag_x} &= \frac{-1}{144(2+\gamma)(2+3\gamma)^2(14+19\gamma)}\left(8K_{fx}^3[14+19\gamma]J_1 + 9K_{fx}J_2\right),\\
F^{(2),x}_{un,ag_z} &= E_1 + K_{fx}^2 J_3,\\
J_1 &= 18+\gamma(45+\gamma(16+\gamma)) - 32\tilde{\rho} - 2\gamma(33+\gamma(12+\gamma))\tilde{\rho}\\
&\quad + (10+\gamma(19+\gamma(8+\gamma)))\tilde{\rho}^2,\\
J_2 &= 28(83+30\tilde{\rho}) + \gamma(7008+3672\tilde{\rho}+\gamma(6551+5658\tilde{\rho}\\
&\quad + \gamma(2010+287\gamma+3504\tilde{\rho}+663\gamma\tilde{\rho}))),\\
J_3 &= \frac{1}{40(2+\gamma)(2+3\gamma)^2(14+19\gamma)}\big[-217\gamma^4(-1+\tilde{\rho})^2 - 2\gamma^3(-1+\tilde{\rho})(-891+665\tilde{\rho})\\
&\quad + \gamma^2(-4609+(7564-2803\tilde{\rho})\tilde{\rho}) - 28(33+\tilde{\rho}(-64+23\tilde{\rho}))\\
&\quad - 8\gamma(471+\tilde{\rho}(-811+288\tilde{\rho}))\big],
\end{aligned} \tag{3.23}$$

and the point torque is obtained as

$$\boldsymbol{T}^x_{un,ag} = 8\pi\mu V_0 R_0^2 \left(\alpha\left[\frac{2-2\gamma(1-\tilde{\rho})+\tilde{\rho}}{8(2+3\gamma)}K_{fx}\hat{\boldsymbol{j}}\right]\right). \tag{3.24}$$

Here, superscript $()^x$ denotes the gravity is in the x-direction. Due to the nonlinearity in the boundary conditions, the point force at $O(\alpha^2)$ in the z-direction depends on the gravitational force in the x-direction, as given in (3.22).

To illustrate the effect of gravitational force orientation on particle deformation, we plotted the deformed shape in an unbounded domain on the xz- and yz-planes when gravity is perpendicular to the particle velocity and is acting in the x-direction. When gravity acts along the x-axis, the shape on the xz- and yz-planes is shown in figures 7(a) and 7(b), respectively. On the plane $y = 0$, the deformed shape remains symmetric about the z-axis in the absence of gravity. However, as shown in figure 7(a), when gravity acts in the x-direction, perpendicular to the velocity of the particle, the deformed shape becomes asymmetric about the z-axis. This causes a shift in the centroid of the particle relative

https://doi.org/10.1017/jfm.2025.10754 Published online by Cambridge University Press

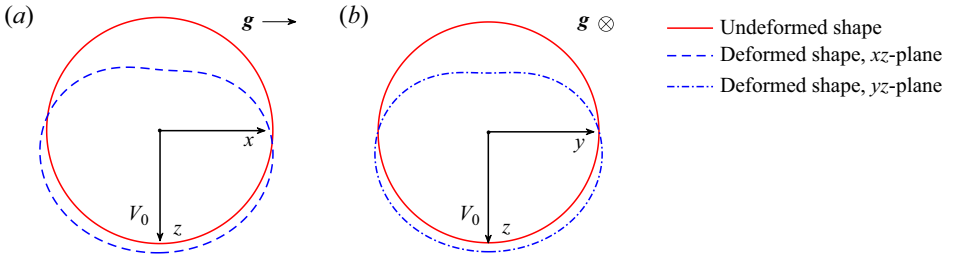


Figure 7. Variation in the shape of the deformed sphere in the unbounded domain at $K_{fx} = 2$, $\alpha = 0.2$, $\gamma = 2$ and $\tilde{\rho} = 1.05$ on the (*a*) xz-plane and (*b*) yz-plane.

to that of the undeformed shape, generating a fluid-induced moment on the particle. This moment is balanced by the external point torque, to make the particle torque-free. However, on the plane $x = 0$, the deformed shape remains symmetric about the z-axis, consistent with the symmetry of the surrounding flow field.

We then analysed the wall effects on the particle dynamics for the arbitrary gravity case. In the presence of the wall, the velocity and displacement fields are calculated at orders $1/H$, α/H and $1/H^2$. The point force until the order we considered is obtained as

$$\boldsymbol{F}_{ag} = \boldsymbol{F}_{un,ag} + 6\pi\mu V_0 R_0 \left[\left(\frac{9}{16H} + \frac{81}{256H^2}\right)\hat{\boldsymbol{k}}\right]. \tag{3.25}$$

The force at $O(\alpha/H)$ is 0 and the point torque is obtained as

$$\boldsymbol{T}_{ag} = \boldsymbol{T}_{un,ag}\left[1 + \frac{9}{16H}\right]. \tag{3.26}$$

The torque at $O(\alpha/H)$ scales as $(\mu^2 V_0^2/G)/(R_0^2/h)$. The first effects of the wall appear as a torque at $O(\alpha/H)$ in this case, as opposed to a lift at $O(\alpha/H^2)$ in the case where gravity is aligned with the particle velocity (3.16).

4. Summary

In this paper, we have investigated the dynamics of a weakly elastic spherical particle translating parallel to a rigid wall in a quiescent fluid in the limit, $\alpha \ll 1$. The motion of the particle is constrained by applying an external point force and point torque. Our model is useful to understand the dynamics of elastic beads embedded with magnetic particles. The analysis is presented for two cases: first, when the gravity is aligned with particle velocity and second, when the gravity is in an arbitrary direction.

For the first case, we have considered three reflections from the wall. The velocity and displacement fields calculated at orders $1/H$, α/H, α^2/H, $1/H^2$, α/H^2 and $1/H^3$ are presented in § 3.1. The external point force needed to make the particle translate in an unbounded domain and parallel to the wall are given in (3.14) and (3.16), respectively. In the unbounded domain, the effects of elasticity appear as a drag at $O(\alpha^2)$, and the external force is aligned with gravity (z-axis). The external point torque is zero until the order we considered in our calculation. A hydrodynamic lift arises due to the wall effects (away from the wall) at $O(\alpha/H^2)$. The scaling of the lift force arises due to the stresslet singularity resulting from the deformation as discussed in § 3.1. The decay rate for the lift force in our calculation scales as $(\mu^2 V_0^2/G)(R_0/h)^2$ and is different from that predicted in the lubrication limit, which scales as $(\mu^2 V_0^2/G)(R_0/h)^{5/2}$ by Skotheim & Mahadevan (2005). We note here that the lateral migration of the deformable particles, such as drops, vesicles

https://doi.org/10.1017/jfm.2025.10754 Published online by Cambridge University Press

or capsules, in bounded simple shear flow is the consequence of the stresslet singularity (Nix *et al.* 2014; Bureau *et al.* 2023). For a neutrally buoyant particle, the force expression (3.17) highlights the emergence of buoyancy force at $O(\alpha^2)$ due to the compressibility of the particle. The expression in the limit of $K_{fz} \ll 1$ is given in (3.19). The force provided in the equation is particularly relevant for microfluidic devices, where one expects $K_{fz} \ll 1$. Figure 2 shows the deformed shape of the particle in the unbounded domain and in the presence of the wall. The deformed shape is symmetric about the translation velocity (z-axis) in the unbounded domain, whereas it is asymmetric in the presence of the wall. The particle shape depends on the density ratio ($\tilde{\rho}$). For a heavier (lighter) particle, increasing K_{fz} reduces (increases) the required external force and decreases (increases) the dip in the particle's upper section seen in figure 3.

For the second case, when gravity and particle velocity are not aligned, we considered two reflections from the wall. The velocity and displacement fields are calculated at orders $1/H$, α/H and $1/H^2$. The external force needed to translate the particle in an unbounded domain is given in (3.20). The force simplifies to (3.22) when gravity acts only in the x-direction. It is important to note that due to nonlinear boundary conditions, the force at $O(\alpha^2)$ in (3.22) acts in the z-direction and depends on the gravitational force in the x-direction. The external force and torque needed to translate the particle parallel to the wall are given in (3.25) and (3.26), respectively. It is noted that for this case, the torque given in (3.21) comes at $O(\alpha)$ in an unbounded domain, which is absent in the first case. Further, the elastic induced wall effects appear as torque at $O(\alpha/H)$ as given in (3.26) for this case, in contrast to lift at $O(\alpha/H^2)$ given in (3.16) for the former case. The analysis we have presented for an arbitrary gravity case can also be used for other body forces such as electric and magnetic forces, by replacing the gravitational force density with an electric or magnetic force density in the definition of K_{px}, K_{py} and K_{pz}, defined following (2.15).

The linearity of Stokes flow allows one to derive a relationship between the hydrodynamic forces and torques on a particle, and its translational and angular velocities through resistance and mobility formulations. The resistance problem, fundamental for determining hydrodynamic forces and torques with prescribed particle velocity, is particularly relevant in scenarios with imposed boundary conditions. Conversely, the mobility problem determines particle motion from applied forces and torques. These formulations are inverse to each other when the particle shape is the same. In both the resistance and mobility problems, the particle is in a state of dynamic equilibrium. To solve the problems, a knowledge of the force distribution that leads to the equilibrium is not needed for a rigid particle; however, in the case of an elastic particle, the knowledge becomes crucial. Notably, the deformed shape of an elastic particle depends on the distribution. The resistance problem of a weakly deformable particle moving parallel to a wall has been solved for both unbounded and semi-infinite domains in this work. In the unbounded case, our results differ from those of Murata (1980), who employs a mobility formulation. While Murata predicts a prolate spheroid shape, our particle shape, shown in figure 2(a), is distinct. The difference arises from the varying force distributions. Further, our approach considers the effect of particle compressibility on density, which is not considered in Murata's analysis when calculating the terminal velocity of the particle. We have revisited Murata's calculation and calculated the terminal velocity considering the density change of the particle, and the results are presented in Appendix D.

Our findings highlight the importance of force distribution in determining the steady-state morphology of deformable particles moving in a fluid. Therefore, identifying the force distribution acting on a deformable particle is essential for analysing its dynamics. The theoretical framework developed in this paper using the point force and the point torque model can be extended to understand the dynamics of magnetoresponsive polymer

https://doi.org/10.1017/jfm.2025.10754 Published online by Cambridge University Press

beads in channels. While in the current work, we model such beads as linearly elastic, such an extension needs the use of nonlinear elastic/viscoelastic models for the bead. The extension will allow one to estimate the magnetic force/torque needed to manipulate the beads in a microchannel.

Funding. This work was supported by funding from Department of Science and Technology India (SERB-Matrices Scheme) and Prime Minister Research Fellowship (PMRF), Ministry of Education India

Declaration of interests. The authors report no conflict of interest.

Appendix A. Solutions to the Navier elasticity equations for a point force and a point torque

The governing equation for an infinite linear, isotropic and homogeneous elastic medium acted upon by a point force at $\boldsymbol{x} = \boldsymbol{0}$ is given by

$$[\lambda + G]\boldsymbol{\nabla}\left(\boldsymbol{\nabla}\cdot\boldsymbol{u}^{pf}\right) + G\boldsymbol{\nabla}^2\boldsymbol{u}^{pf} + \boldsymbol{F}\delta(\boldsymbol{x}) = 0, \tag{A1}$$

where the displacement field ($\boldsymbol{u}^{pf}$) is due to the point force and is given by

$$\begin{aligned}\boldsymbol{u}^{pf}(\boldsymbol{x}) &= \boldsymbol{G}(\boldsymbol{x})\cdot\boldsymbol{F} \\ &= \frac{1}{16(1-\nu)\pi G}\left[\frac{\boldsymbol{I}(3-4\nu)}{r} + \frac{\boldsymbol{x}\boldsymbol{x}}{r^3}\right]\cdot\boldsymbol{F}\,.\end{aligned} \tag{A2}$$

Here, $r = |\boldsymbol{x}|$, $\boldsymbol{G}(\boldsymbol{x})$ is the Green's function and $\nu = \lambda/(2[\lambda + G])$ is the Poisson ratio. It can be shown that (A2) is indeed the solution by substituting it in (A1) and integrating over any volume (V) enclosing point force. Using the divergence theorem, the integration yields

$$\int_V \left([\lambda + G]\boldsymbol{\nabla}\left(\boldsymbol{\nabla}\cdot\boldsymbol{u}^{pf}\right) + G\boldsymbol{\nabla}^2\boldsymbol{u}^{pf}\right)dV = -\boldsymbol{F}\,. \tag{A3}$$

One can derive the displacement field corresponding to a point torque by drawing an analogy to the rotlet singularity in the case of the Stokes equation (Kim & Karrila 2013). The governing equation for an infinite elastic medium with point torque at $\boldsymbol{x} = \boldsymbol{0}$ is given by

$$[\lambda + G]\boldsymbol{\nabla}\left(\boldsymbol{\nabla}\cdot\boldsymbol{u}^{pt}\right) + G\boldsymbol{\nabla}^2\boldsymbol{u}^{pt} + \frac{1}{2}[\boldsymbol{\nabla}\delta(\boldsymbol{x})\times\boldsymbol{T}] = 0\,. \tag{A4}$$

Here, the displacement field ($\boldsymbol{u}^{pt}$) is due to the point torque and is given by

$$\boldsymbol{u}^{pt}(\boldsymbol{x}) = \frac{\boldsymbol{T}\times\boldsymbol{x}}{8\pi G r^3}\,. \tag{A5}$$

One can verify that the displacement field is indeed correct by substituting (A5) in (A4), and taking its moment about the origin and integrating over an arbitrary volume (V) enclosing the point torque. Using the divergence theorem, the integration yields

$$\int_V \boldsymbol{x}\times\left([\lambda + G]\boldsymbol{\nabla}\left(\boldsymbol{\nabla}\cdot\boldsymbol{u}^{pt}\right) + G\boldsymbol{\nabla}^2\boldsymbol{u}^{pt}\right)dV = -\boldsymbol{T}\,. \tag{A6}$$

The displacement field corresponding to the point force and the point torque decays as r^{-1} and r^{-2}, respectively.

https://doi.org/10.1017/jfm.2025.10754 Published online by Cambridge University Press

Appendix B. Gravity aligned with particle velocity

The radial ($v^{(2)}_{un,r}$) and tangential ($v^{(2)}_{un,\theta}$) velocity components at $O(\alpha^2)$ for the case when gravity is in the z-direction are obtained as

$$
\begin{aligned}
v^{(2)}_{un,r} = &-\frac{3\cos\theta}{320(2+\gamma)^2(2+3\gamma)^2(14+19\gamma)\xi^5}[-((-1+\xi^2)(45(-1120\xi^2\\
&+\gamma(368-3440\xi^2)+\gamma^3(1881-860\xi^2)+8\gamma^4(131+4\xi^2)+\gamma^5(177+4\xi^2)\\
&-22\gamma^2(-63+148\xi^2))-60K_{f\tilde{z}}(3\gamma^5(23+28\xi^2)(-1+\tilde{\rho})\\
&-112(2+\xi^2(-3+2\tilde{\rho}))+6\gamma^2(-197+63\tilde{\rho}+6\xi^2(17+6\tilde{\rho}))\\
&+\gamma(-824+92\tilde{\rho}-64\xi^2(-16+7\tilde{\rho}))+\gamma^4(-400+358\tilde{\rho}+8\xi^2(-59+65\tilde{\rho}))\\
&+\gamma^3(-901+570\tilde{\rho}+\xi^2(-516+896\tilde{\rho})))+4K^2_{f\tilde{z}}(\gamma^5(81+244\xi^2)(-1+\tilde{\rho})^2\\
&+8\gamma^4(-1+\tilde{\rho})(-66+39\tilde{\rho}+\xi^2(-109+186\tilde{\rho}))\\
&-4\gamma(-340+586\tilde{\rho}+51\tilde{\rho}^2+4\xi^2(315-349\tilde{\rho}+\tilde{\rho}^2))-56(-4+12\tilde{\rho}+\tilde{\rho}^2\\
&+4\xi^2(6-8\tilde{\rho}+\tilde{\rho}^2))+2\gamma^2(1149-1474\tilde{\rho}-80\tilde{\rho}^2+36\xi^2(-74+54\tilde{\rho}+25\tilde{\rho}^2))\\
&+\gamma^3(3(503-628\tilde{\rho}+68\tilde{\rho}^2)+4\xi^2(-201-499\tilde{\rho}+719\tilde{\rho}^2)))))\\
&+5(9(2800\xi^2+40\gamma(-46+365\xi^2)+8\gamma^4(-655+1319\xi^2)\\
&+\gamma^5(-885+1493\xi^2)+\gamma^3(-9405+25757\xi^2)+\gamma^2(-6930+28498\xi^2))\\
&-12K_{f\tilde{z}}(\gamma^5(-345+649\xi^2)(-1+\tilde{\rho})+560(2+\xi^2(-3+2\tilde{\rho}))\\
&+2\gamma^4(1000-895\tilde{\rho}+\xi^2(-2176+2147\tilde{\rho}))+2\gamma^2(2955-945\tilde{\rho}\\
&+\xi^2(-6439+5563\tilde{\rho}))+\gamma(4120-460\tilde{\rho}+\xi^2(-7456+5732\tilde{\rho}))\\
&+\gamma^3(4505-2850\tilde{\rho})+\xi^2(-10785+10154\tilde{\rho})))\\
&+4K^2_{f\tilde{z}}(\gamma^5(-81+233\xi^2)(-1+\tilde{\rho})^2+8\gamma^4(-1+\tilde{\rho})(66-39\tilde{\rho}\\
&+2\xi^2(-97+93\tilde{\rho}))+56(-4+12\tilde{\rho}+\tilde{\rho}^2+\xi^2(6-20\tilde{\rho}+7\tilde{\rho}^2))\\
&+4\gamma(-340+586\tilde{\rho}+51\tilde{\rho}^2+\xi^2(546-1270\tilde{\rho}+493\tilde{\rho}^2))\\
&+2\gamma^2(-1149+1474\tilde{\rho}+80\tilde{\rho}^2+\xi^2(2221-4430\tilde{\rho}+1894\tilde{\rho}^2))\\
&+\gamma^3(-3(503-628\tilde{\rho}+68\tilde{\rho}^2)+\xi^2(3853-7444\tilde{\rho}+3458\tilde{\rho}^2))))\cos(2\theta)]
\end{aligned}
\tag{B1}
$$

and

$$
\begin{aligned}
v^{(2)}_{un,\theta} = &-\frac{3}{1280(2+\gamma)^2(2+3\gamma)^2(14+19\gamma)\xi^5}[45(560\xi^2(1-4\xi^2)\\
&+\gamma^3(-16929+20275\xi^2-1720\xi^4)+8\gamma^4(-1179+1065\xi^2+8\xi^4)\\
&+\gamma^5(-1593+1147\xi^2+8\xi^4)-8\gamma(414-873\xi^2+860\xi^4)\\
&-2\gamma^2(6237-9607\xi^2+3256\xi^4))-60K_{f\tilde{z}}(\gamma^5(-621+679\xi^2+168\xi^4)(-1+\tilde{\rho})\\
&-112(-18+\xi^2(5-6\tilde{\rho})+\xi^4(-6+4\tilde{\rho}))-4\gamma(\xi^2(940-1163\tilde{\rho})\\
&+32\xi^4(-16+7\tilde{\rho})+9(-206+23\tilde{\rho}))+2\gamma^4(1800-1611\tilde{\rho}\\
&+8\xi^4(-59+65\tilde{\rho})+\xi^2(-2248+2309\tilde{\rho}))+2\gamma^2(5319-1701\tilde{\rho}
\end{aligned}
$$

https://doi.org/10.1017/jfm.2025.10754 Published online by Cambridge University Press

$$
\begin{aligned}
&+ 36\xi^4(17 + 6\tilde{\rho}) + \xi^2(-4645 + 5401\tilde{\rho})) + \gamma^3(8109 - 5130\tilde{\rho} \\
&+ 8\xi^4(-129 + 224\tilde{\rho}) + \xi^2(-10015 + 10806\tilde{\rho}))) \\
&+ 4K_{fz}^2(\gamma^5(-729 + 1491\xi^2 + 488\xi^4)(-1 + \tilde{\rho})^2 \\
&+ 8\gamma^4(-1 + \tilde{\rho})(594 - 351\tilde{\rho} + 24\xi^2(-44 + 51\tilde{\rho}) \\
&+ \xi^4(-218 + 372\tilde{\rho})) - 56(\xi^2(26 + 12\tilde{\rho} - 29\tilde{\rho}^2) \\
&+ 8\xi^4(6 - 8\tilde{\rho} + \tilde{\rho}^2) - 9(-4 + 12\tilde{\rho} + \tilde{\rho}^2)) \\
&- 4\gamma(\xi^2(470 + 2386\tilde{\rho} - 2559\tilde{\rho}^2) + 8\xi^4(315 - 349\tilde{\rho} + \tilde{\rho}^2) \\
&- 9(-340 + 586\tilde{\rho} + 51\tilde{\rho}^2)) + 2\gamma^2(72\xi^4(-74 + 54\tilde{\rho} + 25\tilde{\rho}^2) \\
&+ 9(-1149 + 1474\tilde{\rho} + 80\tilde{\rho}^2) + \xi^2(3479 - 15314\tilde{\rho} + 11430\tilde{\rho}^2)) \\
&+ \gamma^3(-27(503 - 628\tilde{\rho} + 68\tilde{\rho}^2) + 8\xi^4(-201 - 499\tilde{\rho} \\
&+ 719\tilde{\rho}^2) + \xi^2(14639 - 37444\tilde{\rho} + 22634\tilde{\rho}^2))) \\
&+ 5(9(2800\xi^2 + 40\gamma(-138 + 365\xi^2) + 8\gamma^4(-1965 + 1319\xi^2) \\
&+ \gamma^5(-2655 + 1493\xi^2) + \gamma^3(-28215 + 25757\xi^2) + \gamma^2(-20790 + 28498\xi^2)) \\
&- 12K_{fz}(\gamma^5(-1035 + 649\xi^2)(-1 + \tilde{\rho}) + 560(6 + \xi^2(-3 + 2\tilde{\rho})) \\
&+ 4\gamma(3090 - 345\tilde{\rho} + \xi^2(-1864 + 1433\tilde{\rho})) \\
&+ \gamma^4(6000 - 5370\tilde{\rho} + \xi^2(-4352 + 4294\tilde{\rho})) \\
&+ 2\gamma^2(8865 - 2835\tilde{\rho} + \xi^2(-6439 + 5563\tilde{\rho})) \\
&+ \gamma^3(13515 - 8550\tilde{\rho} + \xi^2(-10785 + 10154\tilde{\rho}))) \\
&+ 4K_{fz}^2(\gamma^5(-243 + 233\xi^2)(-1 + \tilde{\rho})^2 \\
&+ 8\gamma^4(-1 + \tilde{\rho})(198 - 117\tilde{\rho} + 2\xi^2(-97 + 93\tilde{\rho})) \\
&+ 56(3(-4 + 12\tilde{\rho} + \tilde{\rho}^2) + \xi^2(6 - 20\tilde{\rho} + 7\tilde{\rho}^2)) \\
&+ 4\gamma(3(-340 + 586\tilde{\rho} + 51\tilde{\rho}^2) + \xi^2(546 - 1270\tilde{\rho} + 493\tilde{\rho}^2)) \\
&+ \gamma^3(-9(503 - 628\tilde{\rho} + 68\tilde{\rho}^2) + \xi^2(3853 - 7444\tilde{\rho} + 3458\tilde{\rho}^2)) \\
&+ \gamma^2(-6894 + 8844\tilde{\rho} + 480\tilde{\rho}^2 + \xi^2(4442 - 8860\tilde{\rho} + 3788\tilde{\rho}^2)))) \cos(2\theta)] \sin\theta.
\end{aligned}
\tag{B2}
$$

The expressions for E_1, E_2, E_3, E_4, I_1, I_2, I_3, I_4 and I_5 in (3.14) and (3.16) for both the unbounded and semi-infinite case are obtained as

$$
E_1 = \frac{9(-140 - 360\gamma - 227\gamma^2 + 6\gamma^3 + \gamma^4)}{8(2+\gamma)(2+3\gamma)^2(14+19\gamma)}, \quad E_2 = \frac{28 + 52\gamma + 19\gamma^2}{9(2+\gamma)(2+3\gamma)^2(14+19\gamma)}, \tag{B3}
$$

$$
E_3 = -\frac{3(7+\gamma)(1+5\gamma)}{5(2+\gamma)}, \quad E_4 = -\frac{9(1708 + 5964\gamma + 6787\gamma^2 + 2850\gamma^3 + 475\gamma^4)}{8(28 + 52\gamma + 19\gamma^2)}, \tag{B4}
$$

$$
I_1 = -\frac{\gamma^3(1-\tilde{\rho})^2 + 8\gamma^2(2 - 3\tilde{\rho} + \tilde{\rho}^2) + 2(9 - 16\tilde{\rho} + 5\tilde{\rho}^2) + \gamma(45 - 66\tilde{\rho} + 19\tilde{\rho}^2)}{2(2+\gamma)}, \tag{B5}
$$

https://doi.org/10.1017/jfm.2025.10754 Published online by Cambridge University Press

$$I_2 = \frac{1}{2(7+\gamma)(1+5\gamma)(14+19\gamma)}\Big[\gamma^3(3102-2162\tilde{\rho}-750\tilde{\rho}^2) + \gamma^2(10734-8569\tilde{\rho}-657\tilde{\rho}^2)+\gamma^4(292-109\tilde{\rho}-183\tilde{\rho}^2) + 28(108-104\tilde{\rho}+3\tilde{\rho}^2)-2\gamma(-5224+4569\tilde{\rho}+18\tilde{\rho}^2)\Big], \tag{B6}$$

$$I_3 = \frac{2044-336\tilde{\rho}-84\gamma(-77+6\tilde{\rho})+6\gamma^3(299+176\tilde{\rho})+\gamma^4(223+252\tilde{\rho})+\gamma^2(6211+576\tilde{\rho})}{1708+5964\gamma+6787\gamma^2+2850\gamma^3+475\gamma^4}, \tag{B7}$$

$$I_4 = \frac{27}{160(28+52\gamma+19\gamma^2)}\Big(\gamma^4(-1+\tilde{\rho})(109+366\tilde{\rho}) + 2\gamma^3(-1407+562\tilde{\rho}+750\tilde{\rho}^2)-56(63+\tilde{\rho}(-64+3\tilde{\rho})) + 2\gamma(-6043+12\tilde{\rho}(454+3\tilde{\rho}))+\gamma^2(-11913+2\tilde{\rho}(4574+657\tilde{\rho}))\Big), \tag{B8}$$

$$I_5 = -\frac{9}{64(2+\gamma)(2+3\gamma)^2(14+19\gamma)}\big(\gamma(7110-756\tilde{\rho})+56(41-9\tilde{\rho}) + 6\gamma^3(223+264\tilde{\rho})+\gamma^4(97+378\tilde{\rho})+\gamma^2(6349+864\tilde{\rho})\big). \tag{B9}$$

The expressions for B_1, B_2, B_3, B_4 and B_5 in (3.15) are obtained as

$$B_1 = \frac{27(5+8\gamma+2\gamma^2)}{32(2+\gamma)(2+3\gamma)},$$

$$B_2 = -\frac{81(7840+33504\gamma+53806\gamma^2+40067\gamma^3+13704\gamma^4+1739\gamma^5)}{512(2+\gamma)^2(2+3\gamma)^2(14+19\gamma)}, \tag{B10}$$

$$B_3 = \frac{27}{256(2+\gamma)^2(2+3\gamma)^2(14+19\gamma)}\Big(647\gamma^5(-1+\tilde{\rho})+224(-11+12\tilde{\rho}) + 4\gamma(-2798+2929\tilde{\rho})+\gamma^4(-4960+5042\tilde{\rho}) + 2\gamma^2(-9353+9587\tilde{\rho})+\gamma^3(-14231+14526\tilde{\rho})\Big), \tag{B11}$$

$$B_4 = -\frac{81(5600+27360\gamma+50066\gamma^2+42109\gamma^3+15864\gamma^4+2101\gamma^5)}{512(2+\gamma)^2(2+3\gamma)^2(14+19\gamma)}, \tag{B12}$$

$$B_5 = \frac{27}{256(2+\gamma)^2(2+3\gamma)^2(14+19\gamma)}\Big(2240(-1+\tilde{\rho})+953\gamma^5(-1+\tilde{\rho}) + 4\gamma(-2698+2751\tilde{\rho})+\gamma^4(-6704+6798\tilde{\rho}) + 2\gamma^2(-9923+10181\tilde{\rho})+\gamma^3(-17065+17458\tilde{\rho})\Big). \tag{B13}$$

Appendix C. Gravity in an arbitrary direction

The expressions for the components of force coefficient at $O(\alpha^2)$ given in (3.20) where gravity is in the arbitrary direction ($\boldsymbol{g} = g_x\hat{\boldsymbol{i}} + g_y\hat{\boldsymbol{j}} + g_z\hat{\boldsymbol{k}}$) are obtained as

$$F^{(2)}_{un,ag_x} = \frac{K_{fx}}{720(2+\gamma)(2+3\gamma)^2(14+19\gamma)}(\gamma[-45\gamma(6551+\gamma(2010+287\gamma)) - 40K_{fz}^2(972+\gamma(1079+\gamma(318+19\gamma)))$$

https://doi.org/10.1017/jfm.2025.10754 Published online by Cambridge University Press

$$
\begin{aligned}
&- 6K_{fz}(30488 + \gamma(29109 + 11\gamma(642 + 47\gamma)))] \\
&+ (80K_{fz}^2(14 + 19\gamma)(16 + \gamma(33 + \gamma(12 + \gamma))) \\
&- 135\gamma(1224 + \gamma(1886 + \gamma(1168 + 221\gamma))) \\
&- 12K_{fz}(-3136 + \gamma(-8544 + \gamma(-5792 + \gamma(344 + 433\gamma)))))\tilde{\rho} \\
&+ 2K_{fz}[-20K_{fz}(14 + 19\gamma)(10 + \gamma(19 + \gamma(8 + \gamma))) \\
&+ 9(532 + \gamma(2352 + \gamma(3679 + \gamma(2330 + 461\gamma))))]\tilde{\rho}^2 \\
&- 36(2905 + 1554K_{fz} + 280K_{fz}^2 + 8760\gamma + 1050\tilde{\rho}) \\
&- 40K_{fx}^2(14 + 19\gamma)(18 + \gamma(45 + \gamma(16 + \gamma)) - 32\tilde{\rho} \\
&- 2\gamma(33 + \gamma(12 + \gamma))\tilde{\rho} + (10 + \gamma(19 + \gamma(8 + \gamma)))\tilde{\rho}^2) \\
&- 40K_{fy}^2(14 + 19\gamma)(18 + \gamma(45 + \gamma(16 + \gamma)) - 32\tilde{\rho} - 2\gamma(33 + \gamma(12 + \gamma))\tilde{\rho} \\
&+ (10 + \gamma(19 + \gamma(8 + \gamma)))\tilde{\rho}^2)), \qquad \text{(C1)}
\end{aligned}
$$

$$
F_{un,ag_y}^{(2)} = \frac{K_{fy}}{K_{fx}}\left[F_{un,ag_x}^{(2)}\right], \qquad \text{(C2)}
$$

$$
\begin{aligned}
F_{un,ag_z}^{(2)} = &-\frac{1}{360(2+\gamma)(2+3\gamma)^2(14+19\gamma)}(8316K_{fy}^2 + 5040K_{fy}^2K_{fz} + 36288K_{fz}^2 \\
&+ 5040K_{fz}^3 + 33912K_{fy}^2\gamma + 291060K_{fz}\gamma + 19440K_{fy}^2K_{fz}\gamma + 125376K_{fz}^2\gamma \\
&+ 19440K_{fz}^3\gamma + 91935\gamma^2 + 41481K_{fy}^2\gamma^2 + 279495K_{fz}\gamma^2 + 21580K_{fy}^2K_{fz}\gamma^2 \\
&+ 128808K_{fz}^2\gamma^2 + 21580K_{fz}^3\gamma^2 - 2430\gamma^3 + 16038K_{fy}^2\gamma^3 + 80730K_{fz}\gamma^3 \\
&+ 6360K_{fy}^2K_{fz}\gamma^3 + 37224K_{fz}^2\gamma^3 + 6360K_{fz}^3\gamma^3 - 405\gamma^4 + 1953K_{fy}^2\gamma^4 \\
&+ 10035K_{fz}\gamma^4 + 380K_{fy}^2K_{fz}\gamma^4 + 3504K_{fz}^2\gamma^4 \\
&+ 380K_{fz}^3\gamma^4 + 180(315 + 511K_{fz} + 810\gamma) \\
&- 2(2K_{fz}(10K_{fz}^2(14 + 19\gamma)(16 + \gamma(33 + \gamma(12 + \gamma))) \\
&- 135(-28 + \gamma(-42 + \gamma(48 + \gamma(88 + 21\gamma)))) \\
&+ 3K_{fz}(2912 + \gamma(9138 + \gamma(8569 + \gamma(2162 + 109\gamma))))) \\
&+ K_{fy}^2(20K_{fz}(14 + 19\gamma)(16 + \gamma(33 + \gamma(12 + \gamma))) \\
&+ 9(896 + \gamma(3244 + \gamma(3782 + \gamma(1556 + 217\gamma))))))\tilde{\rho} \\
&+ (4K_{fz}^2(252 + 5K_{fz}(14 + 19\gamma)(10 + \gamma(19 + \gamma(8 + \gamma))) \\
&- 9\gamma(12 + \gamma(219 + \gamma(250 + 61\gamma)))) \\
&+ K_{fy}^2(20K_{fz}(14 + 19\gamma)(10 + \gamma(19 + \gamma(8 + \gamma))) \\
&+ 9(644 + \gamma(2304 + \gamma(2803 + 7\gamma(190 + 31\gamma))))))\tilde{\rho}^2 \\
&+ K_{fx}^2(20K_{fz}(14 + 19\gamma)(18 + \gamma(45 + \gamma(16 + \gamma)) - 32\tilde{\rho} \\
&- 2\gamma(33 + \gamma(12 + \gamma))\tilde{\rho} + (10 + \gamma(19 + \gamma(8 + \gamma)))\tilde{\rho}^2) \\
&+ 9(217\gamma^4(-1 + \tilde{\rho})^2 + 2\gamma^3(-1 + \tilde{\rho})(-891 + 665\tilde{\rho}) \\
&+ 28(33 + \tilde{\rho}(-64 + 23\tilde{\rho})) + 8\gamma(471 + \tilde{\rho}(-811 + 288\tilde{\rho})) \\
&+ \gamma^2(4609 + \tilde{\rho}(-7564 + 2803\tilde{\rho}))))). \qquad \text{(C3)}
\end{aligned}
$$

https://doi.org/10.1017/jfm.2025.10754 Published online by Cambridge University Press

Appendix D. Modification in the analysis of Murata (1980)

Murata calculated the velocity of a weakly elastic sphere sedimenting under gravity in an unbounded domain. The velocity of the particle ($V_p\hat{\boldsymbol{k}}$) is in the direction of gravity ($g_z\hat{\boldsymbol{k}}$). In our notation, the velocity can be written as an asymptotic series in α as

$$V_p = \frac{2[\tilde{\rho}-1]\rho_f g_z R_0^2}{9\mu}\left[1+\alpha^2 V^{(2)}\right]. \tag{D1}$$

Here, $V^{(2)}$ is the velocity coefficient at $O(\alpha^2)$ and is given by

$$V^{(2)} = \frac{-27\big(6+\gamma[18+\gamma]\big)+6K_{fz}(-1+16\gamma)\tilde{\rho}+8K_{fz}^2\tilde{\rho}^2}{20(2+3\gamma)^2}. \tag{D2}$$

Murata had neglected the density variation of the particle. If one includes that, the coefficient of the terminal velocity at $O(\alpha^2)$ is different from (D2). The modified coefficient at $O(\alpha^2)$ is obtained as

$$V_{mod}^{(2)} = \frac{-243\big(6+\gamma[18+\gamma]\big)+18K_{fz}\big(32+\gamma[133+5\gamma]\big)\tilde{\rho}+6K_{fz}^2(7-50\gamma)\tilde{\rho}^2-20K_{fz}^3\tilde{\rho}^3}{180(2+3\gamma)^2}. \tag{D3}$$

References

ANAND, P. & SUBRAMANIAN, G. 2023 Inertial migration of a sphere in plane couette flow. *J. Fluid Mech.* **977**, A33.

BARTHES-BIESEL, D. 2016 Motion and deformation of elastic capsules and vesicles in flow. *Annu. Rev. Fluid Mech.* **48**, 25–52.

BERTIN, V., AMAROUCHENE, Y., RAPHAËL, E. & SALEZ, T. 2022 Soft-lubrication interactions between a rigid sphere and an elastic wall. *J. Fluid Mech.* **933**, A23.

BUREAU, L., COUPIER, G. & SALEZ, T. 2023 Lift at low reynolds number. *Eur. Phys. J. E* **46** (11), 111.

CHAFFEY, C.E., BRENNER, H. & MASON, S.G. 1965 Particle motions in sheared suspensions: xviii: wall migration (theoretical). *Rheol. Acta* **4** (1), 64–72.

DADDI-MOUSSA-IDER, A., RALLABANDI, B., GEKLE, S. & STONE, H.A. 2018 Reciprocal theorem for the prediction of the normal force induced on a particle translating parallel to an elastic membrane. *Phys. Rev. Fluids* **3** (8), 084101.

DEAN, W.R. & O'NEILL, M.E. 1963 A slow motion of viscous liquid caused by the rotation of a solid sphere. *Mathematika* **10** (1), 13–24.

DODDI, S.K. & P., BAGCHI 2009 Prosenjit 2009 Three-dimensional computational modeling of multiple deformable cells flowing in microvessels. *Phys. Rev. E Stat. Nonlinear Soft Matter Phys.* **79** (4), 046318.

FAXEN, H. 1923 Die bewegung einer starren kugel längs der achse eines mit zäher flüssigkeit gefüllten rohres. *Arkiv Matemetik Astronomi och Fysik* **17**, 1–28.

FINNEY, S.M., HENNESSY, G.M., MÜNCH, A. & WATERS, S.L. 2024 The impact of confinement on the deformation of an elastic particle under axisymmetric tube flow. *Ima J. Appl. Math.* **89** (3), 498–532.

GOLDMAN, A.J., COX, R.G. & BRENNER, H. 1967 Slow viscous motion of a sphere parallel to a plane wall – I motion through a quiescent fluid. *Chem. Eng. Sci.* **22** (4), 637–651.

GUAZZELLI, E. & MORRIS, J.F. 2011 *A Physical Introduction to Suspension Dynamics*. vol. 45. Cambridge University Press.

HO, B.P. & LEAL, L.G. 1974 Inertial migration of rigid spheres in two-dimensional unidirectional flows. *J. Fluid Mech.* **65** (2), 365–400.

JOHNS, L.E. & NARAYANAN, R. 2002 *Interfacial Instability*. Springer Science & Business Media.

KARGAR-ESTAHBANATI, A. & RALLABANDI, B. 2021 Lift forces on three-dimensional elastic and viscoelastic lubricated contacts. *Phys. Rev. Fluids* **6** (3), 034003.

KIM, B.-S., QIU, J.-M., WANG, J.-P. & TATON, T.A. 2005 Magnetomicelles: composite nanostructures from magnetic nanoparticles and cross-linked amphiphilic block copolymers. *Nano Lett.* **5** (10), 1987–1991.

KIM, S. & KARRILA, S.J. 2013 *Microhydrodynamics: Principles and Selected Applications*. Courier Corporation.

KUSHCH, V. 2013 *Micromechanics of Composites: Multipole Expansion Approach*. Butterworth-Heinemann.

https://doi.org/10.1017/jfm.2025.10754 Published online by Cambridge University Press

LEAL, L.G. 1980 Particle motions in a viscous fluid. *Annu. Rev. Fluid Mech.* **12**, 435–476.
LEAL, L.G. 2007 *Advanced Transport Phenomena: Fluid Mechanics and Convective Transport Processes*. Cambridge University Press.
LI, S., YU, H., LI, T.-D., CHEN, Z., DENG, W., ANBARI, A. & FAN, J. 2020 Understanding transport of an elastic, spherical particle through a confining channel. *Appl. Phys. Lett.* **116** (10), 103705.
MAGNAUDET, J., TAKAGI, S.H.U. & LEGENDRE, D. 2003 Drag, deformation and lateral migration of a buoyant drop moving near a wall. *J. Fluid Mech.* **476**, 115–157.
MAŁYSA, K. & VAN DE VEN, T.G.M. 1986 Rotational and translational motion of a sphere parallel to a wall. *Int. J. Multiphas. Flow* **12** (3), 459–468.
MATAS, J.P., MORRIS, J.F. & GUAZZELLI, E. 2004 Lateral forces on a sphere. *Oil Gas Sci. Technol.* **59** (1), 59–70.
MOERLAND, C.P., VAN IJZENDOORN, L.J. & PRINS, M.W.J.2019 Rotating magnetic particles for lab-on-chip applications – a comprehensive review. *Lab Chip* **19** (6), 919–933.
MURATA, T. 1980 On the deformation of an elastic particle falling in a viscous fluid. *J. Phys. Soc. Japan* **48** (5), 1738–1745.
MURATA, T. 1981 Deformation of an elastic particle suspended in an arbitrary flow field. *J. Phys. Soc. Japan* **50** (3), 1009–1016.
NAKAYAMA, S., YAMASHITA, H., YABU, T., ITANO, T. & SUGIHARA-SEKI, M. 2019 Three regimes of inertial focusing for spherical particles suspended in circular tube flows. *J. Fluid Mech.* **871**, 952–969.
NASOURI, B., KHOT, A. & ELFRING, G.J. 2017 Elastic two-sphere swimmer in stokes flow. *Phys. Rev. Fluids* **2** (4), 043101.
NIX, S., IMAI, Y., MATSUNAGA, D., YAMAGUCHI, T. & ISHIKAWA, T. 2014 Lateral migration of a spherical capsule near a plane wall in stokes flow. *Phys. Rev. E* **90** (4), 043009.
NOICHL, I. & SCHÖNECKER, C. 2022 Dynamics of elastic, nonheavy spheres sedimenting in a rectangular duct. *Soft Matt.* **18** (12), 2462–2472.
O'NEILL, M.E. 1964 A slow motion of viscous liquid caused by a slowly moving solid sphere. *Mathematika* **11** (1), 67–74.
PENG, S., ZHANG, M., NIU, X., WEN, W., SHENG, P., LIU, Z. & SHI, J. 2008 Magnetically responsive elastic microspheres. *Appl. Phys. Lett.* **92** (1).
PHILIPPOVA, O., BARABANOVA, A., MOLCHANOV, V. & KHOKHLOV, A. 2011 Magnetic polymer beads: recent trends and developments in synthetic design and applications. *Eur. Polym. J.* **47** (4), 542–559.
RALLABANDI, B. 2024 Fluid-elastic interactions near contact at low reynolds number. *Annu. Rev. Fluid Mech.* **56** (1), 491–519.
RALLABANDI, B., OPPENHEIMER, N., ZION, B., YAH, M. & STONE, H.A. 2018 Membrane-induced hydroelastic migration of a particle surfing its own wave. *Nat. Phys.* **14** (12), 1211–1215.
RALLABANDI, B., SAINTYVES, B., JULES, T., SALEZ, T., SCHÖNECKER, C., MAHADEVAN, L. & STONE, H.A. 2017 Rotation of an immersed cylinder sliding near a thin elastic coating. *Phys. Rev. Fluids* **2** (7), 074102.
SAFARIK, I., SAFARIKOVA, M. & FORSYTHE, S.J. 1995 The application of magnetic separations in applied microbiology.
SAFARIKOVA, M. & SAFARIK, I. 2001 The application of magnetic techniques in biosciences. *Phys. Separation Sci. Engine* **10** (4), 223–252.
SAFFMAN, P.G. 1965 The lift on a small sphere in a slow shear flow. *J. Fluid Mech.* **22** (2), 385–400.
SAINTYVES, B., JULES, T., SALEZ, T. & MAHADEVAN, L. 2016 Self-sustained lift and low friction via soft lubrication. *Proc. Natl. Acad. Sci.* **113** (21), 5847–5849.
SECOMB, T.W., SKALAK, R., ÖZKAYA, N. & GROSS, J.F. 1986 Flow of axisymmetric red blood cells in narrow capillaries. *J. Fluid Mech.* **163**, 405–423.
SEGRE, G. & SILBERBERG, A. 1961 Radial particle displacements in poiseuille flow of suspensions. *Nature* **189** (4760), 209–210.
SEKIMOTO, K. & LEIBLER, L. 1993 A mechanism for shear thickening of polymer-bearing surfaces: elasto-hydrodynamic coupling. *Europhys. Lett.* **23** (2), 113.
SKOTHEIM, J.M. & MAHADEVAN, L. 2005 Soft lubrication: the elastohydrodynamics of nonconforming and conforming contacts. *Phys. Fluids* **17** (9).
SONG, Y., LI, D. & XUAN, X. 2023 Recent advances in multi-mode microfluidic separation of particles and cells. *Electrophoresis*.
TAM, C.K.W. & HYMAN, W.A. 1973 Transverse motion of an elastic sphere in a shear field. *J. Fluid Mech.* **59** (1), 177–185.
URZAY, J., SMITH, L., STEFAN, G. & GLOVER, B.J. 2007 The elastohydrodynamic force on a sphere near a soft wall. *Phys. Fluids* **19** (10).

https://doi.org/10.1017/jfm.2025.10754 Published online by Cambridge University Press

VASSEUR, P. & COX, R.G. 1976 The lateral migration of a spherical particle in two-dimensional shear flows. *J. Fluid Mech.* **78** (2), 385–413.

VILLONE, M.M. & MAFFETTONE, P.L. 2019 Dynamics, rheology, and applications of elastic deformable particle suspensions: a review. *Rheol. Acta* **58**, 109–130.

WU, T., YANG, Z., HU, R., CHEN, Y.-F., ZHONG, H., YANG, L. & JIN, W. 2021 Film entrainment and microplastic particles retention during gas invasion in suspension-filled microchannels. *Water Res.* **194**, 116919.

https://doi.org/10.1017/jfm.2025.10754 Published online by Cambridge University Press